DESY–07–011
February 2007

Leading neutron energy and p_T distributions in deep inelastic scattering and photoproduction at HERA

ZEUS Collaboration

Abstract

The production of energetic neutrons in *ep* collisions has been studied with the ZEUS detector at HERA. The neutron energy and p_T^2 distributions were measured with a forward neutron calorimeter and tracker in a $40\,\text{pb}^{-1}$ sample of inclusive deep inelastic scattering (DIS) data and a $6\,\text{pb}^{-1}$ sample of photoproduction data. The neutron yield in photoproduction is suppressed relative to DIS for the lower neutron energies and the neutrons have a steeper p_T^2 distribution, consistent with the expectation from absorption models. The distributions are compared to HERA measurements of leading protons. The neutron energy and transverse-momentum distributions in DIS are compared to Monte Carlo simulations and to the predictions of particle exchange models. Models of pion exchange incorporating absorption and additional secondary meson exchanges give a good description of the data.

The ZEUS Collaboration

S. Chekanov[1], M. Derrick, S. Magill, S. Miglioranzi[2], B. Musgrave, D. Nicholass[2], J. Repond, R. Yoshida
Argonne National Laboratory, Argonne, Illinois 60439-4815, USA [n]

M.C.K. Mattingly
Andrews University, Berrien Springs, Michigan 49104-0380, USA

M. Jechow, N. Pavel [†], A.G. Yagües Molina
Institut für Physik der Humboldt-Universität zu Berlin, Berlin, Germany

S. Antonelli, P. Antonioli, G. Bari, M. Basile, L. Bellagamba, M. Bindi, D. Boscherini, A. Bruni, G. Bruni, L. Cifarelli, F. Cindolo, A. Contin, M. Corradi[3], S. De Pasquale, G. Iacobucci, A. Margotti, R. Nania, A. Polini, L. Rinaldi, G. Sartorelli, A. Zichichi
University and INFN Bologna, Bologna, Italy [e]

D. Bartsch, I. Brock, S. Goers[4], H. Hartmann, E. Hilger, H.-P. Jakob, M. Jüngst, O.M. Kind, E. Paul[5], R. Renner, U. Samson, V. Schönberg, R. Shehzadi, M. Wlasenko
Physikalisches Institut der Universität Bonn, Bonn, Germany [b]

N.H. Brook, G.P. Heath, J.D. Morris, T. Namsoo
H.H. Wills Physics Laboratory, University of Bristol, Bristol, United Kingdom [m]

M. Capua, S. Fazio, A. Mastroberardino, M. Schioppa, G. Susinno, E. Tassi
Calabria University, Physics Department and INFN, Cosenza, Italy [e]

J.Y. Kim[6], K.J. Ma[7]
Chonnam National University, Kwangju, South Korea [g]

Z.A. Ibrahim, B. Kamaluddin, W.A.T. Wan Abdullah
Jabatan Fizik, Universiti Malaya, 50603 Kuala Lumpur, Malaysia [r]

Y. Ning, Z. Ren, F. Sciulli
Nevis Laboratories, Columbia University, Irvington on Hudson, New York 10027 [o]

J. Chwastowski, A. Eskreys, J. Figiel, A. Galas, M. Gil, K. Olkiewicz, P. Stopa, L. Zawiejski
The Henryk Niewodniczanski Institute of Nuclear Physics, Polish Academy of Sciences, Cracow, Poland [i]

L. Adamczyk, T. Bołd, I. Grabowska-Bołd, D. Kisielewska, J. Łukasik, M. Przybycień, L. Suszycki
Faculty of Physics and Applied Computer Science, AGH-University of Science and Technology, Cracow, Poland [p]

A. Kotański[8], W. Słomiński
Department of Physics, Jagellonian University, Cracow, Poland

V. Adler, U. Behrens, I. Bloch, C. Blohm, A. Bonato, K. Borras, N. Coppola, A. Dossanov, J. Fourletova, A. Geiser, D. Gladkov, P. Göttlicher[9], I. Gregor, T. Haas, W. Hain, C. Horn, B. Kahle, U. Klein[10], U. Kötz, H. Kowalski, E. Lobodzinska, B. Löhr, R. Mankel, I.-A. Melzer-Pellmann, A. Montanari, D. Notz, A.E. Nuncio-Quiroz, I. Rubinsky, R. Santamarta, U. Schneekloth, A. Spiridonov[11], H. Stadie, D. Szuba[12], J. Szuba[13], T. Theedt, G. Wolf, K. Wrona, C. Youngman, W. Zeuner
Deutsches Elektronen-Synchrotron DESY, Hamburg, Germany

W. Lohmann, S. Schlenstedt
Deutsches Elektronen-Synchrotron DESY, Zeuthen, Germany

G. Barbagli, E. Gallo, P. G. Pelfer
University and INFN, Florence, Italy [e]

A. Bamberger, D. Dobur, F. Karstens, N.N. Vlasov[14]
Fakultät für Physik der Universität Freiburg i.Br., Freiburg i.Br., Germany [b]

P.J. Bussey, A.T. Doyle, W. Dunne, J. Ferrando, D.H. Saxon, I.O. Skillicorn
Department of Physics and Astronomy, University of Glasgow, Glasgow, United Kingdom [m]

I. Gialas[15]
Department of Engineering in Management and Finance, Univ. of Aegean, Greece

T. Gosau, U. Holm, R. Klanner, E. Lohrmann, H. Salehi, P. Schleper, T. Schörner-Sadenius, J. Sztuk, K. Wichmann, K. Wick
Hamburg University, Institute of Exp. Physics, Hamburg, Germany [b]

C. Foudas, C. Fry, K.R. Long, A.D. Tapper
Imperial College London, High Energy Nuclear Physics Group, London, United Kingdom [m]

M. Kataoka[16], T. Matsumoto, K. Nagano, K. Tokushuku[17], S. Yamada, Y. Yamazaki
Institute of Particle and Nuclear Studies, KEK, Tsukuba, Japan [f]

A.N. Barakbaev, E.G. Boos, N.S. Pokrovskiy, B.O. Zhautykov
Institute of Physics and Technology of Ministry of Education and Science of Kazakhstan, Almaty, Kazakhstan

D. Son
Kyungpook National University, Center for High Energy Physics, Daegu, South Korea [g]

J. de Favereau, K. Piotrzkowski
Institut de Physique Nucléaire, Université Catholique de Louvain, Louvain-la-Neuve, Belgium [q]

F. Barreiro, C. Glasman[18], M. Jimenez, L. Labarga, J. del Peso, E. Ron, M. Soares, J. Terrón, M. Zambrana
Departamento de Física Teórica, Universidad Autónoma de Madrid, Madrid, Spain [l]

F. Corriveau, C. Liu, R. Walsh, C. Zhou
Department of Physics, McGill University, Montréal, Québec, Canada H3A 2T8 [a]

T. Tsurugai
Meiji Gakuin University, Faculty of General Education, Yokohama, Japan [f]

A. Antonov, B.A. Dolgoshein, V. Sosnovtsev, A. Stifutkin, S. Suchkov
Moscow Engineering Physics Institute, Moscow, Russia [j]

R.K. Dementiev, P.F. Ermolov, L.K. Gladilin, I.I. Katkov, L.A. Khein, I.A. Korzhavina, V.A. Kuzmin, B.B. Levchenko[19], O.Yu. Lukina, A.S. Proskuryakov, L.M. Shcheglova, D.S. Zotkin, S.A. Zotkin
Moscow State University, Institute of Nuclear Physics, Moscow, Russia [k]

I. Abt, C. Büttner, A. Caldwell, D. Kollar, W.B. Schmidke, J. Sutiak
Max-Planck-Institut für Physik, München, Germany

G. Grigorescu, A. Keramidas, E. Koffeman, P. Kooijman, A. Pellegrino, H. Tiecke, M. Vázquez[16], L. Wiggers
NIKHEF and University of Amsterdam, Amsterdam, Netherlands [h]

N. Brümmer, B. Bylsma, L.S. Durkin, A. Lee, T.Y. Ling
Physics Department, Ohio State University, Columbus, Ohio 43210 [n]

P.D. Allfrey, M.A. Bell, A.M. Cooper-Sarkar, A. Cottrell, R.C.E. Devenish, B. Foster, K. Korcsak-Gorzo, S. Patel, V. Roberfroid[20], A. Robertson, P.B. Straub, C. Uribe-Estrada, R. Walczak
Department of Physics, University of Oxford, Oxford United Kingdom [m]

P. Bellan, A. Bertolin, R. Brugnera, R. Carlin, R. Ciesielski, F. Dal Corso, S. Dusini, A. Garfagnini, S. Limentani, A. Longhin, L. Stanco, M. Turcato
Dipartimento di Fisica dell' Università and INFN, Padova, Italy [e]

B.Y. Oh, A. Raval, J. Ukleja[21], J.J. Whitmore[22]
Department of Physics, Pennsylvania State University, University Park, Pennsylvania 16802 [o]

Y. Iga
Polytechnic University, Sagamihara, Japan [f]

G. D'Agostini, G. Marini, A. Nigro
Dipartimento di Fisica, Università 'La Sapienza' and INFN, Rome, Italy [e]

J.E. Cole, J.C. Hart
Rutherford Appleton Laboratory, Chilton, Didcot, Oxon, United Kingdom [m]

H. Abramowicz[23], A. Gabareen, R. Ingbir, S. Kananov, A. Levy
Raymond and Beverly Sackler Faculty of Exact Sciences, School of Physics, Tel-Aviv University, Tel-Aviv, Israel [d]

M. Kuze
Department of Physics, Tokyo Institute of Technology, Tokyo, Japan [f]

R. Hori, S. Kagawa[24], N. Okazaki, S. Shimizu, T. Tawara
Department of Physics, University of Tokyo, Tokyo, Japan [f]

R. Hamatsu, H. Kaji[25], S. Kitamura[26], O. Ota, Y.D. Ri
Tokyo Metropolitan University, Department of Physics, Tokyo, Japan [f]

M.I. Ferrero, V. Monaco, R. Sacchi, A. Solano
Università di Torino and INFN, Torino, Italy [e]

M. Arneodo, M. Ruspa
Università del Piemonte Orientale, Novara, and INFN, Torino, Italy [e]

S. Fourletov, J.F. Martin
Department of Physics, University of Toronto, Toronto, Ontario, Canada M5S 1A7 [a]

S.K. Boutle[15], J.M. Butterworth, C. Gwenlan[27], T.W. Jones, J.H. Loizides, M.R. Sutton[27], C. Targett-Adams, M. Wing
Physics and Astronomy Department, University College London, London, United Kingdom [m]

B. Brzozowska, J. Ciborowski[28], G. Grzelak, P. Kulinski, P. Łużniak[29], J. Malka[29], R.J. Nowak, J.M. Pawlak, T. Tymieniecka, A. Ukleja[30], A.F. Żarnecki
Warsaw University, Institute of Experimental Physics, Warsaw, Poland

M. Adamus, P. Plucinski[31]
Institute for Nuclear Studies, Warsaw, Poland

Y. Eisenberg, I. Giller, D. Hochman, U. Karshon, M. Rosin
Department of Particle Physics, Weizmann Institute, Rehovot, Israel [c]

E. Brownson, T. Danielson, A. Everett, D. Kçira, D.D. Reeder[5], P. Ryan, A.A. Savin, W.H. Smith, H. Wolfe
Department of Physics, University of Wisconsin, Madison, Wisconsin 53706, USA [n]

S. Bhadra, C.D. Catterall, Y. Cui, G. Hartner, S. Menary, U. Noor, J. Standage, J. Whyte
Department of Physics, York University, Ontario, Canada M3J 1P3 [a]

[1] supported by DESY, Germany
[2] also affiliated with University College London, UK
[3] also at University of Hamburg, Germany, Alexander von Humboldt Fellow
[4] self-employed
[5] retired
[6] supported by Chonnam National University in 2005
[7] supported by a scholarship of the World Laboratory Björn Wiik Research Project
[8] supported by the research grant no. 1 P03B 04529 (2005-2008)
[9] now at DESY group FEB, Hamburg, Germany
[10] now at University of Liverpool, UK
[11] also at Institut of Theoretical and Experimental Physics, Moscow, Russia
[12] also at INP, Cracow, Poland
[13] on leave of absence from FPACS, AGH-UST, Cracow, Poland
[14] partly supported by Moscow State University, Russia
[15] also affiliated with DESY
[16] now at CERN, Geneva, Switzerland
[17] also at University of Tokyo, Japan
[18] Ramón y Cajal Fellow
[19] partly supported by Russian Foundation for Basic Research grant no. 05-02-39028-NSFC-a
[20] EU Marie Curie Fellow
[21] partially supported by Warsaw University, Poland
[22] This material was based on work supported by the National Science Foundation, while working at the Foundation.
[23] also at Max Planck Institute, Munich, Germany, Alexander von Humboldt Research Award
[24] now at KEK, Tsukuba, Japan
[25] now at Nagoya University, Japan
[26] Department of Radiological Science
[27] PPARC Advanced fellow
[28] also at Łódź University, Poland
[29] Łódź University, Poland
[30] supported by the Polish Ministry for Education and Science grant no. 1 P03B 12629
[31] supported by the Polish Ministry for Education and Science grant no. 1 P03B 14129

[†] deceased

[a] supported by the Natural Sciences and Engineering Research Council of Canada (NSERC)

[b] supported by the German Federal Ministry for Education and Research (BMBF), under contract numbers HZ1GUA 2, HZ1GUB 0, HZ1PDA 5, HZ1VFA 5

[c] supported in part by the MINERVA Gesellschaft für Forschung GmbH, the Israel Science Foundation (grant no. 293/02-11.2) and the U.S.-Israel Binational Science Foundation

[d] supported by the German-Israeli Foundation and the Israel Science Foundation

[e] supported by the Italian National Institute for Nuclear Physics (INFN)

[f] supported by the Japanese Ministry of Education, Culture, Sports, Science and Technology (MEXT) and its grants for Scientific Research

[g] supported by the Korean Ministry of Education and Korea Science and Engineering Foundation

[h] supported by the Netherlands Foundation for Research on Matter (FOM)

[i] supported by the Polish State Committee for Scientific Research, grant no. 620/E-77/SPB/DESY/P-03/DZ 117/2003-2005 and grant no. 1P03B07427/2004-2006

[j] partially supported by the German Federal Ministry for Education and Research (BMBF)

[k] supported by RF Presidential grant N 8122.2006.2 for the leading scientific schools and by the Russian Ministry of Education and Science through its grant Research on High Energy Physics

[l] supported by the Spanish Ministry of Education and Science through funds provided by CICYT

[m] supported by the Particle Physics and Astronomy Research Council, UK

[n] supported by the US Department of Energy

[o] supported by the US National Science Foundation. Any opinion, findings and conclusions or recommendations expressed in this material are those of the authors and do not necessarily reflect the views of the National Science Foundation.

[p] supported by the Polish Ministry of Science and Higher Education

[q] supported by FNRS and its associated funds (IISN and FRIA) and by an Inter-University Attraction Poles Programme subsidised by the Belgian Federal Science Policy Office

[r] supported by the Malaysian Ministry of Science, Technology and Innovation/Akademi Sains Malaysia grant SAGA 66-02-03-0048

1 Introduction

In ep scattering at HERA, a significant fraction of events contains a low-transverse-momentum baryon carrying a large fraction of the incoming proton energy [1–5]. Although the production mechanism of these leading baryons is not completely understood, exchange models (Fig. 1) give a reasonable description of the data. In this picture, the incoming proton emits a virtual particle which scatters on the photon emitted from the beam electron. The outgoing baryon, of energy E_B, carries a fraction $x_L = E_B/E_p$ of the beam energy, while the exchanged particle participates in the process with energy $(1 - x_L)E_p$.

In particular, one-pion exchange is a significant contributor to leading neutron production for large x_L [1, 2]. For such a process the cross section for the semi-inclusive reaction $\gamma^* p \to Xn$ factorizes into two terms (Regge factorization [6]):

$$\frac{d^2\sigma(W^2, Q^2, x_L, t)}{dx_L dt} = f_{\pi/p}(x_L, t)\sigma_{\gamma^*\pi}((1 - x_L)W^2, Q^2),$$

where Q^2 is the virtuality of the exchanged photon, W is the center-of-mass energy of the virtual photon-proton system and t is the square of the four-momentum of the exchanged pion. In terms of the measured quantities x_L and transverse momentum p_T, the pion virtuality is:

$$t \simeq -\frac{p_T^2}{x_L} - \frac{(1 - x_L)(m_n^2 - m_p^2 x_L)}{x_L}.$$

The flux of virtual pions emitted by the proton is represented by $f_{\pi/p}$ and $\sigma_{\gamma^*\pi}$ is the cross section of the virtual-photon and virtual-pion interaction at center-of-mass energy $\sqrt{1 - x_L}\,W$. If the $\gamma^*\pi$ cross section is independent of t, the p_T distribution of produced neutrons is completely determined by the flux factor.

Many parameterizations of the pion flux have been suggested in the literature [6–11]. They have the general form:

$$f_{\pi/p}(x_L, t) \propto \frac{-t}{(t - m_\pi^2)^2}(1 - x_L)^{\alpha(t)} F^2(x_L, t).$$

The power $\alpha(t)$ and the form factor $F(x_L, t)$ are model dependent with parameters that can be extracted from hadron-hadron scattering data.

Comparisons between cross sections for the production of particles in the fragmentation region of a target nucleon provide tests of the concepts of vertex factorization and limiting fragmentation [12]. The hypothesis of limiting fragmentation states that, in the high-energy limit, the production of particles in the proton target-fragmentation region is independent of the nature of the incident projectile. For leading neutron production in

ep scattering, where the projectile is the exchanged virtual photon, this implies that the dependence of the cross section on the lepton variables (W, Q^2) should be independent of the baryon variables (x_L, t). For such vertex factorization, the cross section can be written as

$$\frac{d^2\sigma(W^2, Q^2, x_L, p_T^2)}{dx_L dp_T^2} = g(x_L, p_T^2) G(W^2, Q^2),$$

where g and G are arbitrary functions. The Regge factorization introduced earlier violates this vertex factorization because of the dependence of $\sigma_{\gamma^*\pi}$ on x_L in addition to W^2 and Q^2. Factorization tests involve comparing semi-inclusive rates, normalized to their respective total cross sections, to study whether particle production from a given target is independent of the lepton variables.

In exchange models, neutron absorption can occur through rescattering [13–16]. In a geometrical picture [14], if the size of the n-π system is small compared to the size of the photon, the neutron can also scatter on the photon. The neutron may migrate to lower x_L and higher p_T such that it is outside of the detector acceptance. The rescattering can also transform the neutron into a charged baryon which may also escape detection. Since the size of the virtual photon is inversely related to Q^2, more neutron rescattering would be expected for photoproduction ($Q^2 \approx 0$) than for deep inelastic scattering (DIS, $Q^2 \gtrsim 1\,\text{GeV}^2$). A previous study [2] showed a mild violation of vertex factorization with the expected increase of rate when going from photoproduction to DIS. Similar effects have also been seen for leading protons [3]. The size of the n-π system is inversely proportional to the neutron p_T, so rescattering removes neutrons with large p_T. Thus rescattering results in a depletion of high p_T neutrons in photoproduction relative to DIS: a violation of vertex factorization. Pion-exchange models [6–11] incorporate a variation of the mean size of the n-π system as a function of x_L. This results in an x_L dependence of the absorption, again a violation of vertex factorization.

Absorption is a key ingredient in calculations of gap-survival probability in pp interactions at the LHC, critical in interpreting hard diffractive processes, including central exclusive Higgs production. The most recent absorption model calculations [15,16], based on multi-Pomeron exchanges, gave a good description of previous leading-neutron results on absorption [2].

This paper presents measurements of the x_L and p_T^2 distributions of leading neutrons coming from samples of DIS and photoproduction (γp) processes, with more than seven times higher statistics and smaller systematic uncertainties than the previous ZEUS publication [2]. The x_L and p_T^2 distributions in DIS and photoproduction are compared as a test of vertex factorization. The neutron measurements are compared to similar measurements of leading protons at HERA. The data are also compared to the predictions of several Monte Carlo (MC) models. The neutron p_T^2 distributions in DIS are compared to several pion-exchange models with various choices of their parameters. Finally, the x_L and p_T distributions in photoproduction and DIS are compared to models incorporating pion exchange and rescattering, and a model that also includes secondary meson exchanges.

2 Detectors

A detailed description of the ZEUS detector can be found elsewhere [17]. A brief outline of the components that are most relevant for this analysis is given below.

The high-resolution uranium–scintillator calorimeter (CAL) [18] consists of three parts: the forward (FCAL), the barrel (BCAL) and the rear (RCAL) calorimeters. Each part is subdivided transversely into towers and longitudinally into one electromagnetic section (EMC) and either one (in RCAL) or two (in BCAL and FCAL) hadronic sections (HAC). The smallest subdivision of the calorimeter is called a cell. The CAL energy resolutions, as measured under test-beam conditions, are $\sigma(E)/E = 0.18/\sqrt{E}$ for electrons and $\sigma(E)/E = 0.35/\sqrt{E}$ for hadrons (E in GeV). The EMC sections were used to detect scattered positrons in DIS events and the RCAL was used to trigger on the dissociated photon in photoproduction events.

Bremsstrahlung, $ep \rightarrow e\gamma p$, and the photoproduction of hadrons, $ep \rightarrow eX$, are tagged using the luminosity detectors [19]. The bremsstrahlung photons are measured with a lead-scintillator calorimeter located at $Z = -107\,\mathrm{m}$[1] from the interaction point in the positron-beam direction. The positron tagger was a similar calorimeter at $Z = -35\,\mathrm{m}$ from the interaction point with an energy resolution of $\sigma(E)/E = 0.19/\sqrt{E}$ (E in GeV). It was used to measure positrons scattered at very small angles in an energy range of 5-20 GeV.

The forward neutron calorimeter (FNC) [20] was installed in the HERA tunnel at $\theta = 0$ degrees and at $Z = 106\,\mathrm{m}$ from the interaction point in the proton-beam direction, as depicted in Fig. 2. It was used for the 1995-2000 data taking. The FNC was a lead-scintillator calorimeter with an energy resolution for hadrons measured in a test beam to be $\sigma(E)/E = 0.70/\sqrt{E}$ (E in GeV). The calorimeter was segmented vertically into 14 towers as shown in Fig. 3. Three planes of veto counters were located in front of the FNC to reject events in which a particle showered in dead material along the beamline upstream of the FNC.

In 1998 a forward neutron tracker (FNT) was installed in the FNC at a depth of one

---

[1] The ZEUS coordinate system is a right-handed Cartesian system, with the Z axis pointing in the proton beam direction, referred to as the “forward direction”, and the X axis pointing towards the center of HERA. The coordinate origin is at the nominal interaction point.

interaction length. It was a scintillator hodoscope designed to measure the position of neutron showers. Each scintillator finger was 16.8 cm long, 1.2 cm wide and 0.5 cm deep; 17 were used for X position reconstruction and 15 for Y. Figure 3 shows the position of the FNT hodoscope in the FNC relative to the incoming neutron beam. The irregular outlined area indicates the geometric acceptance defined by magnet apertures. This limited detection to neutrons with production angles less than 0.75 mrad, allowing transverse momenta in the range $p_T \leq E_n \theta_{\max} = 0.69\, x_L\,\mathrm{GeV}$. The resulting kinematic regions in p_T^2 and t are shown in Fig. 4.

Scans by a ^{60}Co radioactive source and data from frequent proton beam-gas runs were used to calibrate and monitor both detectors. The relative calibration between FNC towers was adjusted using position information from the FNT. The energy scale of the FNC was determined with a systematic uncertainty of ±2% from fits to the endpoint of the neutron energy spectrum near 920 GeV. The minimum-ionizing-particle (mip) scale in the veto counters was determined by selecting electromagnetic showers in the FNC, a large fraction of which were converted photons which deposited a 2-mip signal in the counters. The position resolution of neutron showers in the FNT of ±0.23 cm was measured by placing an adjustable collimator in front of the outermost veto counter of the FNC during special test and calibration runs.

3 Data selection and analysis

The data for this analysis were collected in 2000 when HERA collided 27.5 GeV positrons with 920 GeV protons, giving an ep center-of-mass energy $\sqrt{s} = 318\,\mathrm{GeV}$. Separate triggers were used to collect DIS and photoproduction events with leading neutrons.

3.1 Data selection

The DIS events were collected using a trigger that required the detection of the scattered positron in the CAL. In the offline analysis, the scattered positron was required to have energy $E'_e > 10\,\mathrm{GeV}$ and to be at least 3 cm from the inner edge of the beam-pipe hole in the RCAL. The quantity $E - P_Z = \sum_i E_i(1 - \cos\theta_i)$, with the sum running over all calorimeter cells, was required to be in the range $35 < E - P_Z < 65\,\mathrm{GeV}$; the lower cut reduced photoproduction background with a misidentified positron. These cuts resulted in a clean sample of DIS events in the kinematic range $Q^2 > 2\,\mathrm{GeV}^2$ with a mean photon virtuality of $\langle Q^2 \rangle \simeq 13\,\mathrm{GeV}^2$. For further studies, the variable Q^2 was reconstructed using the double angle (DA) method [21]. This method requires a certain amount of hadronic activity in the CAL in order to measure the angle of the hadronic system. To ensure this, an additional requirement $y_{\rm JB} > 0.02$ was imposed for those measurements requiring Q^2 reconstruction. Here $y_{\rm JB}$ is the inelasticity $y \approx (W^2 + Q^2)/s$ reconstructed using the Jacquet-Blondel (JB) method [22]. The integrated luminosity of the DIS sample was approximately $40\,\text{pb}^{-1}$.

The photoproduction events were collected during the last part of the 2000 running period using a trigger that required at least 5 GeV in the positron tagger in coincidence with at least 464 MeV in the RCAL EMC [23]. The acceptance of the positron tagger limited the photon virtuality to $Q^2 < 0.02\,\text{GeV}^2$, with a mean Q^2 of approximately $\langle Q^2 \rangle \simeq 4 \times 10^{-4}\,\text{GeV}^2$. Offline, the total energy per event deposited in the photon tagger was required to be less than 1 GeV in order to reject overlapping bremsstrahlung events. The integrated luminosity of the photoproduction sample was approximately $6\,\text{pb}^{-1}$.

The DIS and photoproduction triggers required at least 180 GeV of energy to be deposited in the FNC. Good FNC neutron candidates were required offline to satisfy the following conditions:

- the FNC tower with maximum energy was one of the four towers covered by the FNT as depicted in Fig. 3, to reject protons with $x_L < 1$ which were deflected into the top towers of the FNC by the vertical bending magnets shown in Fig. 2;
- the veto counter had a signal of less than one mip, to reject showers which started in dead material upstream of the FNC; to minimize effects of backsplash from hadronic showers, only the veto counter farthest from the FNC was used;
- no signal in the veto counter consistent with a shower from a previous bunch crossing, to reject pile-up energy deposits;
- the timing information from the FNC consistent with the triggered bunch;
- energy sharing among the towers was used to reject electromagnetic showers from high-energy photons.

These cuts, similar to those used in the previous ZEUS measurements [2,5], selected long-lived neutral hadrons which had not interacted with material before reaching the FNC. The sample was predominantly neutrons, with a small component of K_L^0 hadrons. The MC models Rapgap with pion exchange [24] and Lepto with soft color interactions [25] predict that the K_L^0 contribution is less than 2% above $x_L = 0.6$, and increases slowly to approximately 20% at $x_L = 0.2$.

The above selection was used for the x_L measurements. For results requiring also a measurement of p_T^2, the following additional requirements were imposed to ensure a well reconstructed position measurement in the FNT:

- the highest pulse-height channel in each of the hodoscope planes was above the pedestal level, to select neutrons which showered before the FNT plane;

- shower profiles with more than one peak were rejected, to eliminate mismeasurement from shower fluctuations.

The fraction of clean FNC neutrons passing the FNT cuts determined the FNT efficiency as a function of x_L. The efficiency rises with neutron energy from 35% at $x_L = 0.2$ to 63% at $x_L = 0.85$, corresponding to the fraction of neutrons that shower before the FNT.

3.2 Normalization

The cross sections for leading neutron production presented here, σ_{LN}, were normalized to the inclusive cross sections without a leading-neutron requirement, σ_{inc}, as:

$$r_{\text{LN}}(W^2, Q^2) = \frac{\sigma_{\text{LN}}(W^2, Q^2)}{\sigma_{\text{inc}}(W^2, Q^2)}.$$

Variations of this relative neutron yield, r_{LN}, with W^2 or Q^2 indicate differences in the neutron-production mechanism. The acceptance for detecting different types of events in the central ZEUS detector in a small kinematic region of (W^2, Q^2) is independent of the neutron requirement; the acceptance cancels in the yield r_{LN}, so that:

$$r_{\text{LN}}(W^2, Q^2) = \frac{N_{\text{LN}}(W^2, Q^2)}{N_{\text{inc}}(W^2, Q^2)}.$$

Here N_{inc} is the number of inclusive events in the sample and N_{LN} is the number of these events with a neutron tag, corrected for the acceptance of the forward neutron detectors. The acceptance of the central ZEUS detector varies with (W^2, Q^2); if the neutron-tagged and inclusive events have different kinematic dependences, their acceptances integrated over a given (W^2, Q^2) region would be different. The mild violation of vertex factorization observed in the previous ZEUS measurement [2] indicates that such differences in acceptance are less than 2%, and so were ignored. Thus the acceptance of the central ZEUS detector and associated systematic uncertainties do not affect the neutron yield. Only the acceptance of the forward neutron detectors together with its systematic uncertainties are relevant for measuring r_{LN}.

For the DIS sample, a set of inclusive events was collected simultaneously and used to normalize the neutron data. For the inclusive photoproduction events, $49\,\text{nb}^{-1}$ of data were collected in a special run in 1996 when the proton beam energy was 820 GeV, for measurement of the photon-proton total cross section [23]. The normalization of the 2000 photoproduction data was determined by assuming that the ratio of the photoproduction and DIS neutron yields, for any given neutron (x_L, p_T^2) kinematic region, was the same at the two proton beam energies:

$$\left.\frac{r_{\text{LN}}^{\gamma p}}{r_{\text{LN}}^{\text{DIS}}}\right|_{920\,\text{GeV}} = \left.\frac{r_{\text{LN}}^{\gamma p}}{r_{\text{LN}}^{\text{DIS}}}\right|_{820\,\text{GeV}}.$$

In this equation $r_{\mathrm{LN}}^{\gamma p}(820\,\mathrm{GeV})$ was measured in the 1996 inclusive photoproduction sample, $r_{\mathrm{LN}}^{\mathrm{DIS}}(820\,\mathrm{GeV})$ was measured in inclusive DIS data from the same running period and $r_{\mathrm{LN}}^{\mathrm{DIS}}(920\,\mathrm{GeV})$ was measured in the inclusive DIS data from the 2000 running period. The neutron kinematic region for the measured yields was $x_L > 0.2$ and $p_T^2 < 0.476\,x_L^2\,\mathrm{GeV}^2$. This normalization procedure resulted in an uncertainty on the neutron yield in photoproduction of 5.1%, predominantly from the limited statistics of the 1996 photoproduction data.

3.3 Beamline and forward-detector simulation

The acceptance of the forward neutron detectors, for the measurement of neutron yields, was determined from a simple one-particle MC simulation. The simulation accounts for the aperture and dead material along the neutron flight path, the measured proton beam position and p_T spread, and the measured detector resolutions.

Figure 5 shows a scatter plot of reconstructed hits in the FNT from a sample of DIS events. The irregular curve is the aperture expected from the MC simulation. Numerous events are reconstructed outside of the aperture, as the aperture is not a sharp boundary as modeled, but presents a varying amount of dead material over several millimeters transverse to the neutron flight path. The effect of this on the measured neutron yield is less than 2% and was ignored.

The simulation also modeled significant amounts of dead material along the neutron flight path, primarily from stations S5 and S6 of the ZEUS leading proton spectrometer (LPS) shown in Fig. 2. The LPS was a set of Roman pots used to measure protons scattered at very low angles [26]. The elements of these stations were measured after the LPS was removed from the HERA tunnel in 2000 and implemented in the simulation. The positions of these elements in the simulation were adjusted to reproduce the data. For example, the deficit of events observed near $Y \sim 10.5\,\mathrm{cm}$, seen clearly in the vertical slice of the scatter plot in Fig. 6, determined the vertical alignment of the LPS. There is good agreement between the simulation and the data distributions.

During operation, the LPS was normally in one of two positions: extracted, or inserted for data taking. Separate dead material maps were made for the two positions. Data collected during periods when the LPS was moving were rejected. The results were determined separately for the two LPS positions and combined according to the luminosity taken in each position. The difference with the results obtained for each position was taken as a measure of the systematic uncertainty from the dead material map.

The reconstruction of the neutron scattering angle, θ_n, requires knowledge of the zero-degree point. This was determined by generating a symmetric distribution of neutrons, passing it through the simulation, and fitting the reconstructed distribution to the data. An example of such a fit for the zero-degree position in the vertical plane is shown in Fig. 6. Considering different input distributions, and taking into account the uncertainties in the dead material map, the beam zero-degree point was determined to an accuracy of ± 0.2 cm in both X and Y.

The simulation also takes into account the energy resolution of the FNC, the position resolution of the FNT, and the inherent p_T-spread of the HERA proton beam. The latter was measured in the reaction $\gamma p \rightarrow \rho p$, with the ρ decay products measured in the ZEUS central detector and the final-state proton measured with the LPS [26]. The beam p_T-spread corresponds to a smearing of the zero-degree point by 0.45 cm horizontally and 1.0 cm vertically, significantly larger than the FNT resolution. The spectrum of generated neutrons was tuned to match the x_L and p_T^2 distributions separately for the DIS and photoproduction samples.

These MC distributions were then used to correct the data for all acceptance and smearing effects. For distributions requiring a position measurement, the correction for the x_L-dependent FNT efficiency was also applied.

3.4 Systematic uncertainties

The dominant effects contributing to the systematic uncertainties arose from:

- the beam zero-degree point;
- the dead material map;
- the FNC energy scale;
- the p_T^2 distributions, input for x_L-distribution acceptance.

The systematic uncertainties were typically 5–10% of the measured quantities, and are shown as shaded bands in the figures. The variation of the energy scale shifted the points in x_L. The other systematic variations amount to a change in acceptance resulting in a correlated shift of the neutron yields. The small uncertainties from the assumption of acceptance cancellation in $r_{\rm LN}$ and from the aperture edge were ignored.

Corrections for efficiency of the cuts and backgrounds were applied to the normalization of the neutron yields. The corrections, similar to those of the previous ZEUS measurement [2], were:

- false veto counter firing: $+10.6 \pm 1.0\%$, determined from randomly triggered events;
- veto counter inefficiency: $-2.5 \pm 1.0\%$, determined from 2-mip distributions in the veto counter;

- backsplash from neutron showers: $+1.5 \pm 1.5\%$, determined from timing information in the veto counter giving the fraction of late time vetoes;
- neutrons from proton beam-gas interactions: $-1.4 \pm 0.3\%$, determined from randomly triggered events.

The overall systematic uncertainty on the normalization of the neutron yield from these corrections, not included in the shaded bands of the figures, was $\pm 2.1\%$. The yield in photoproduction has an additional uncertainty of $\pm 5.1\%$ from the normalization procedure described in Section 3.2.

4 Results

4.1 Neutron x_L and p_T^2 distributions in DIS

Figure 7 shows the normalized differential distribution $(1/\sigma_{\rm inc}) d\sigma_{\rm LN}/dx_L$ for neutrons in DIS with scattering angles $\theta_n < 0.75\,$mrad, corresponding to the kinematic range $p_T^2 < 0.476\, x_L^2\,{\rm GeV}^2$. It rises from the lowest x_L due to the increase in p_T^2 space, reaches a maximum near $x_L = 0.7$, and falls to zero at the endpoint $x_L = 1$. These results are consistent with the previous ZEUS measurement [2]. Integrating this distribution, the total leading-neutron yield for the measured region is:

$$r_{\rm LN}(Q^2 > 2\,{\rm GeV}^2, x_L > 0.2, p_T^2 < 0.476\, x_L^2\,{\rm GeV}^2) = 0.0885 \pm 0.0002\,({\rm stat.})\,^{+0.0034}_{-0.0029}\,({\rm sys.}).$$

Here the systematic uncertainty includes the overall $\pm 2.1\%$ scale uncertainty.

The corrected p_T^2 distributions in DIS for different x_L bins are shown in Fig. 8 and summarized in Table 1. They are presented as normalized doubly differential distributions $(1/\sigma_{\rm inc}) d^2\sigma_{\rm LN}/dx_L dp_T^2$. The bins in p_T^2 are at least as large as the resolution, which is dominated by the p_T spread of the proton beam. The varying p_T^2 ranges of the plots are due to the aperture limitation. The line on each plot is a fit to the functional form $d\sigma_{\rm LN}/dp_T^2 \propto \exp(-bp_T^2)$. The distributions are compatible with a single exponential within the statistical and uncorrelated systematic uncertainties. Thus, with the parameterization

$$\frac{1}{\sigma_{\rm inc}} \frac{d^2\sigma_{\rm LN}}{dx_L dp_T^2} = a(x_L)\, e^{-b(x_L)p_T^2},$$

the neutron (x_L, p_T^2) distribution is fully characterized by the slopes $b(x_L)$ and intercepts $a(x_L) = (1/\sigma_{\rm inc}) d^2\sigma_{\rm LN}/dx_L dp_T^2|_{p_T^2=0}$. The dependences of the intercepts and the slopes on x_L are shown in Figs. 9 and 10 and summarized in Table 2. The systematic uncertainties were evaluated by making the variations listed in Section 3.4 and repeating the fits. The intercepts fall rapidly from the lowest x_L, are roughly constant in the region $x_L = 0.45$-0.75, and fall to zero at the endpoint $x_L = 1$. Below $x_L = 0.32$, the slopes are consistent with zero and are not plotted; they rise linearly in the range $0.3 < x_L < 0.85$ to a value of $b \simeq 8\,\mathrm{GeV}^{-2}$, and then decrease slightly at higher x_L. Figure 11 shows the ratio a/b for the region $0.32 < x_L < 1$ where $b > 0$, which can be taken as the leading-neutron yield integrated over p_T^2 values from zero to infinity, assuming that the p_T^2 distributions remain an exponential also beyond the measured p_T^2 range. This distribution, integrated over x_L in the range $0.32 < x_L < 1$, corresponds to a yield:

$$r_{\mathrm{LN}}(Q^2 > 2\,\mathrm{GeV}^2, x_L > 0.32) = 0.159 \pm 0.008\,(\mathrm{stat.})\,^{+0.019}_{-0.006}\,(\mathrm{sys.}).$$

Here the systematic uncertainty includes the overall 2.1% scale uncertainty.

4.2 Q^2 dependence of leading neutron production

To investigate the Q^2 dependence of leading-neutron production, the full DIS sample was divided into three subsamples depending on the Q^2_{DA} range, with the additional cut $y_{\mathrm{JB}} > 0.02$. The kinematic regions in Q^2 and W for all DIS and photoproduction samples are summarized in Table 3.

Figure 12 shows the x_L distributions and Fig. 13 the p_T^2 slopes in the range $p_T^2 < 0.476\,x_L^2\,\mathrm{GeV}^2$ for the photoproduction and three DIS subsamples. There is a trend of increasing neutron yield with increasing Q^2, a clear violation of vertex factorization. There is a large increase between the photoproduction region and the low- and mid-Q^2 DIS regions, in which the data are nearly Q^2 independent. There is then a smaller, but significant, increase between the mid-Q^2 and high-Q^2 regions. The effect of the different W ranges for the DIS and photoproduction samples on the neutron yield was less than 5%, as evaluated by restricting the DIS sample to low- and high-W regions. The slopes for all three DIS samples are equal within the uncertainties. The slopes for photoproduction are higher in the region $0.6 < x_L < 0.9$.

The total neutron yields integrated over $x_L > 0.2$ for the four samples are summarized in Table 4. The doubly differential distributions $1/\sigma_{\mathrm{inc}} d\sigma_{LN}/dx_L dp_T^2$ for the photoproduction and three DIS subsamples are summarized in Table 5, and the intercepts and slopes of the exponential fits are summarized in Table 6.

To investigate the differences between the photoproduction and DIS regimes further, the effects of energy calibration and beam position drifts were minimized by using only the subset of DIS data collected simultaneously with the photoproduction data. The DIS sample without y_{JB} or Q^2_{DA} cuts was used to maximize the statistical precision of the comparison.

The ratio of the normalized differential distributions

$$\rho(x_L) = \frac{\dfrac{1}{\sigma_{\rm inc}^{\gamma p}}\dfrac{d\sigma_{\rm LN}^{\gamma p}}{dx_L}}{\dfrac{1}{\sigma_{\rm inc}^{\rm DIS}}\dfrac{d\sigma_{\rm LN}^{\rm DIS}}{dx_L}}$$

for the region $p_T^2 < 0.476\,x_L^2\,{\rm GeV}^2$ is shown in Fig. 14. In the range $0.2 < x_L < 0.4$, the ratio drops slightly but rises for higher x_L values, exceeding unity for $x_L > 0.9$. The deviation of the ratio from unity is a clear violation of vertex factorization. The ratio of the intercepts for photoproduction and DIS, which has a nearly identical behavior to that of Fig. 14, is not shown.

The p_T^2 distributions for both samples, normalized to unity at $p_T^2 = 0$, are shown in Fig. 15. The photoproduction distributions are steeper in the range $0.6 < x_L < 0.9$, with relatively fewer neutrons at high p_T^2. The difference of the slopes $\Delta b = b(Q^2 < 0.02\,{\rm GeV}^2) - b(Q^2 > 2\,{\rm GeV}^2)$ is less sensitive to systematic effects than each of the individual slopes. These values are plotted in Fig. 16. The slopes for photoproduction are larger in the range $0.6 < x_L < 0.9$, with $\Delta b = 0.5$–$1.0\ {\rm GeV}^{-2}$, qualitatively consistent with the violation of vertex factorization expected from absorption as discussed in the introduction.

4.3 Comparison to leading protons

ZEUS has also reported x_L distributions for leading protons in the kinematic region $p_T^2 < 0.04\,{\rm GeV}^2$ [4]. The neutron x_L distributions were also measured in the same region, using the FNT measurement of p_T^2. The results for DIS are compared in Fig. 17. There are approximately twice as many protons as neutrons in the range $0.6 < x_L < 0.9$. If only isospin-1 particle exchanges contributed to proton production, there should be half as many protons as neutrons. Thus, exchanges of particles with different isospins such as isoscalars must be invoked to account for the observed proton rate [11].

The slopes of the p_T^2 distributions for leading protons and neutrons in DIS are shown in Fig. 18. Note that the p_T^2 range for the proton measurement, $p_T^2 < 0.5\,{\rm GeV}^2$, is larger than for the neutron measurement. The two samples have similar values of b near $x_L \approx 0.8$, the region where pion exchange is expected to dominate for both processes [11].

5 Comparison to models

In this section the data are compared to several models. First the data are compared to various MC models for the simulation of DIS events. A comparison is then made to models incorporating only pion exchange. Next, more sophisticated models including the effects of absorption of the neutron are considered. Finally, a model incorporating enhanced absorption with pion and additional secondary Regge exchanges is discussed.

5.1 Monte Carlo models

Most MC models generate leading neutrons from the fragmentation of the proton remnant [27]. Some models also incorporate additional processes to simulate diffraction and leading baryon production. The leading neutron x_L distribution, intercepts and slopes in DIS are compared to two MC models in Fig. 19. The models presented here are RAPGAP [24] and LEPTO [28]. The proton PDF parameterization used was CTEQ5L [29]. With only standard proton-remnant fragmentation, the models are lower than the data in the normalization of the x_L distribution and intercepts, and are peaked at lower x_L. They do not show the observed x_L dependence of the slopes. Other models incorporating only standard fragmentation, ARIADNE [30] and CASCADE [31] for DIS, and PYTHIA [32] and PHOJET [33] for photoproduction, give a similarly poor description of the data.

LEPTO has the option to implement soft color interactions (SCI) [25] to produce rapidity gaps observed in diffractive events. This model gives a qualitative description of the leading proton x_L distribution [4], including the diffractive peak, although it predicts too few protons in the central x_L region. The predictions for leading neutrons, with the probability of SCI set to 0.5, are shown in Fig. 19. LEPTO SCI comes close to the data in the shape and normalization of the x_L distribution. The intercepts also exhibit a shoulder in the distribution near $x_L \approx 0.8$ similar to that in the data. It does not, however, give the observed strong x_L dependence of the slopes.

RAPGAP also includes Pomeron exchange to simulate diffractive events, and pion exchange to simulate leading baryon production. These processes are mixed with standard fragmentation according to their respective cross sections. The PDF parameterizations used here were the H1 LO fit 2 [34] for the Pomeron and GRV-P LO fit [35] for the pion. The predictions for leading neutrons from a mixture of these exchanges and standard fragmentation are also shown in Fig. 19. The model well reproduces the shape of the x_L distribution and intercepts, although it predicts more neutrons than are observed. The model also shows the strong x_L dependence of the slopes in the data, although the predicted values of the slopes are systematically larger than the data.

5.2 Pure pion exchange

In the Regge factorization relation discussed in the introduction, the leading neutron x_L distribution is a product of the pion flux, $f_{\pi/p}$, and the $\gamma^*\pi$ cross section, $\sigma_{\gamma^*\pi}$. However, if $\sigma_{\gamma^*\pi}$ is assumed to be independent of t, the p_T distribution of the produced neutrons is determined only by the pion flux $f_{\pi/p}$. The slopes can be compared to various parameterizations of the flux. Although $f_{\pi/p}$ is not an exponential in p_T^2, at fixed x_L the models can be fit to the form $\exp(-bp_T^2)$ using the same binning as the data, and the resulting $b(x_L)$ values compared to the measurements. All of the parameterizations in the literature [6–9, 11] give values for the slopes larger than the data. Most of them also have the wrong x_L dependence of the slopes. The models that most resemble the data are shown in Fig. 20. The simple model of Bishari [6], with the form factor $F(x_L, t) = 1$, is closest in magnitude to the data. Other models with more detailed parameterizations show the turnover of the slopes near $x_L \approx 0.85$ [7]. The model of Holtmann et al. [8] is used for pion exchange in the RAPGAP-π MC. The values for b from RAPGAP-π in Fig. 19 are lower than this curve because RAPGAP also includes a contribution from standard fragmentation, which has flatter p_T^2 distributions than pion exchange. None of these models, based on pion exchange alone, describes the data.

5.3 Pion exchange with neutron absorption

As discussed in the introduction, in a geometrical picture, neutron absorption may occur for large photon sizes and small n-π separations. The former is inversely related to Q^2, and so is largest for photoproduction; thus more absorption is expected in photoproduction than in DIS. The n-π separation $r_{n\pi}$ is the Fourier conjugate of p_T, and the distribution of $r_{n\pi}$ is given by the Fourier transform of $f_{\pi/p}(p_T)$. Parameterizations of the pion flux in general show that the mean value of $r_{n\pi}$ increases with x_L, so more absorption is expected at lower x_L than at higher x_L. The dashed curve in Fig. 21 is the expectation for the suppression of leading neutrons in photoproduction relative to DIS from a model of pion exchange with neutron absorption [14]. Although the curve lies below the data, it follows the same trend. The γp interaction has a power-law dependence $\sigma \propto W^{2\lambda}$, with different values of λ for DIS and photoproduction. Assuming that $\gamma\pi$ interactions have the same dependence, and recalling that $W_{\gamma\pi} = \sqrt{1 - x_L} W_{\gamma p}$, the ratio of photoproduction and DIS cross sections is proportional to $(1 - x_L)^{\Delta\lambda}$. Previous ZEUS measurements of λ in photoproduction [23] and DIS [36, 37] give $\Delta\lambda \approx -0.13$. Applying this to the absorption suppression factor results in the solid curve in Fig. 21. Within the normalization uncertainty of 5.1%, the data are well described by the absorption model with this correction for different W dependences. Hence such a geometric absorption model can account for the differences between the x_L distributions in DIS and photoproduction.

Also shown in Fig. 21 is the NSZ model [13] which employs the optical theorem together with multi-Pomeron exchanges to describe all possible rescattering processes of the leading hadron, resulting in absorptive effects. With the correction for different W

dependences, the prediction is close in magnitude to the data, but does not have as steep an x_L dependence.

5.4 Enhanced neutron absorption and secondary exchanges

Recently a new calculation (KKMR) of pion exchange with neutron absorption based on multi-Pomeron exchanges has become available [15]. The pion exchange is based on the Bishari flux. In addition to the rescatterings implemented in the earlier model [13], a small contribution from rescattering on intermediate partons in the central rapidity region is also included. The model also accounts for the migration of neutrons in (x_L, p_T^2) after rescattering. The prediction for the neutron x_L distribution for photoproduction, where rescattering is most important, is shown by the dashed curve in Fig. 22. The model gives a fair description of both the shape and normalization of the data. The loss of neutrons through absorption is approximately 50%; this is consistent with the deviation from the $\sigma_{\gamma\pi}/\sigma_{\gamma p} = 2/3$ prediction of the additive quark model that was noted in the previous ZEUS measurement [2]. Within this model, the present data can be used to constrain the gap-survival probability, one of the crucial inputs to calculations of diffractive interactions at the LHC — both hard, such as central exclusive Higgs production, and soft, such as those giving rise to the diffractive pile-up events [38]. The prediction of this model for the slopes b in DIS is shown in Fig. 23. As for the pure pion-exchange calculations, the model predicts larger values of b than seen in the data. This model does give a fair prediction for the magnitude of the difference of the slopes in photoproduction and DIS, as shown in Fig. 23.

More recently this model was extended to include, in addition to pion exchange, the exchange of secondary (ρ, a_2) Reggeons [16]. This extended model gives a fair description of the shape and normalization of the x_L distribution in photoproduction, as seen in Fig. 22. Since there are additional exchanges the model gives a prediction for the x_L distribution which is higher than for pion-exchange alone. As shown in Fig. 23, the model with secondary exchanges also gives a good prediction for the slopes. Its description of the slope differences is also close in magnitude to the data, as seen in Fig. 23.

6 Summary

The x_L and p_T^2 distributions of leading neutrons in photoproduction and DIS events at HERA have been measured. The x_L distributions for the measured region $\theta_n < 0.75\,\mathrm{mrad}$ rise from the lowest x_L due to the increasing p_T phase space, reach a maximum near $x_L = 0.7$, and fall to zero at the endpoint $x_L = 1$. The p_T^2 distributions are well described by an exponential $d\sigma/dp_T^2 = a\exp(-bp_T^2)$. The intercepts a fall rapidly from the lowest x_L, are roughly constant in the region $x_L = 0.45$-0.75, and fall to zero at the endpoint $x_L = 1$. The exponential slopes b rise linearly with x_L in the range $0.3 < x_L < 0.85$ to a value of $b \simeq 8\,\text{GeV}^{-2}$, and then decrease slightly at higher x_L.

The neutron yield rises monotonically with Q^2 from the photoproduction region $Q^2 < 0.02\,\text{GeV}^2$ to the high-Q^2 DIS region $Q^2 > 20\,\text{GeV}^2$. The relative rise in yield is greatest near $x_L = 0.5$ and becomes less significant at higher x_L. The slopes of the p_T^2 distributions do not change significantly within the DIS region $Q^2 > 2\,\text{GeV}^2$, but the slopes in photoproduction exhibit a small increase over those in DIS for $0.6 < x_L < 0.9$.

In the kinematic region $0.6 < x_L < 0.9$ and $p_T^2 < 0.04\,\text{GeV}^2$ there are approximately twice as many leading protons as neutrons. This indicates that leading proton production proceeds through exchanges in addition to pure isovector (e.g. pion) exchange. The slopes b for leading protons agree with the neutron slopes near $x_L \approx 0.8$ where pion exchange is expected to dominate both processes.

Monte Carlo models commonly in use for the simulation of DIS and photoproduction events which implement standard fragmentation of the proton remnant do not describe the leading-neutron data. They predict fewer neutrons, concentrated at lower x_L. They also predict smaller p_T^2 slopes and do not have the strong x_L dependence of the data. The inclusion of soft color interactions gives a reasonable description of the x_L distributions, but again fails to predict the p_T^2 slopes. A mixture of processes including standard fragmentation, diffraction and pion exchange gives a good description of the x_L distributions and the x_L dependence of the slopes, although they are larger than the data.

The measured $b(x_L)$ dependence in DIS has been compared with various pion-exchange models. All models give values larger than the data. The simplest model is closest in magnitude to the data; other models reproduce the measured shape of $b(x_L)$.

The Q^2 dependence of the neutron yield and p_T^2 slopes is consistent with absorption models where neutrons from pion exchange with smaller n-π separations are lost through rescattering on larger photons. The photon size increases with decreasing Q^2, and the mean n-π separation is smaller in the mid-x_L range than at higher x_L. The result is a depletion of neutrons with decreasing Q^2, with the depletion greater at mid-x_L than at higher x_L, as seen in the data. The loss of neutrons with small n-π separations, corresponding to large p_T^2, also explains the larger p_T^2 slopes measured in photoproduction than in DIS.

A model of neutron production through pion exchange, incorporating enhanced neutron absorption and migration of the neutrons in (x_L, p_T^2) after rescattering, gives a fair description of the shape and normalization of the x_L distributions in DIS and photoproduction, and of the difference in the p_T^2 slopes b between the two sets. However, as with pure pion exchange, it predicts too high a value for b. Extending the model to include also ρ and a_2 exchanges still gives a fair description of the shape and normalization of the x_L distributions in DIS and photoproduction, and also good descriptions of the p_T^2 slopes and of the differences between the two sets.

Acknowledgements

We are especially grateful to the DESY Directorate whose encouragement and financial support made possible the construction and installation of the FNC. We are also happy to acknowledge the DESY accelerator group for allowing the installation of the FNC in close proximity to the HERA machine components. We also acknowledge the support of the DESY computing staff.

We thank V. Khoze, A. Martin and M. Ryskin for valuable discussions and for providing the results of their calculations.

References

[1] ZEUS Coll., M. Derrick et al., Phys. Lett. **B 384**, 388 (1995);
H1 Coll., C. Adloff et al., Eur. Phys. J. **C 6**, 587 (1999).

[2] ZEUS Coll., J. Breitweg et al., Nucl. Phys. **B 637**, 3 (2002).

[3] H1 Coll., C. Adloff et al., Nucl. Phys. **B 619**, 3 (2001);
H1 Coll., A. Aktas et al., Eur. Phys. J. **C 41**, 273 (2005).

[4] ZEUS Coll., J. Breitweg et al., Nucl. Phys. **B 658**, 3 (2003).

[5] ZEUS Coll., J. Breitweg et al., Nucl. Phys. **B 596**, 3 (2001);
ZEUS Coll., S. Chekanov et al., Phys. Lett. **B 590**, 143 (2004);
ZEUS Coll., S. Chekanov et al., Phys. Lett. **B 610**, 199 (2005).

[6] M. Bishari, Phys. Lett. **B 38**, 510 (1972).

[7] L.L. Frankfurt, L. Mankiewicz and M.I. Strikman, Z. Phys. **A 334**, 343 (1989);
K. Golec-Biernat, J. Kwiecinski and A. Szczurek, Phys. Rev. **D 56**, 3955 (1997).

[8] H. Holtmann et al., Phys. Lett. **B 338**, 363 (1994).

[9] B. Kopeliovich, B. Povh and I. Potashnikova, Z. Phys. **C 73**, 125 (1996);
M. Przybycien, A. Szczurek and G. Ingelman, Z. Phys. **C 74**, 509 (1997);
W. Melnitchouk, J. Speth and A.W. Thomas, Phys. Rev. **D 59**, 014033 (1998).

[10] N.N. Nikolaev et al., Phys. Rev. **D 60**, 014004 (1999).

[11] A. Szczurek, N.N. Nikolaev and J. Speth, Phys. Lett. **B 428**, 383 (1998).

[12] J. Benecke et al., Phys. Rev. **188**, 2159 (1969);
T.T. Chou and C.N. Yang, Phys. Rev. **D 50**, 590 (1994).

[13] N.N. Nikolaev, J. Speth and B.G. Zakharov, Preprint KFA-IKP(TH)-1997-17 (hep-ph/9708290), KFA-IKP, 1997.

[14] U. D'Alesio and H.J. Pirner, Eur. Phys. J. **A 7**, 109 (2000).

[15] A.B. Kaidalov et al., Eur. Phys. J. **C 47**, 385 (2006).

[16] V.A. Khoze, A.D. Martin and M.G. Ryskin, Preprint IPPP-06-36, DCPT-06-72 (hep-ph/0606213), 2006.

[17] ZEUS Coll., U. Holm (ed.), *The ZEUS Detector*. Status Report (unpublished), DESY (1993), available on `http://www-zeus.desy.de/bluebook/bluebook.html`.

[18] M. Derrick et al., Nucl. Inst. Meth. **A 309**, 77 (1991);
A. Andresen et al., Nucl. Inst. Meth. **A 309**, 101 (1991);
A. Caldwell et al., Nucl. Inst. Meth. **A 321**, 356 (1992);
A. Bernstein et al., Nucl. Inst. Meth. **A 336**, 23 (1993).

[19] J. Andruszków et al., Preprint DESY-92-066, DESY, 1992;
ZEUS Coll., M. Derrick et al., Z. Phys. **C 63**, 391 (1994);
J. Andruszków et al., Acta Phys. Pol. **B 32**, 2025 (2001).

[20] S. Bhadra et al., Nucl. Inst. Meth. **A 354**, 479 (1995);
ZEUS Coll., FNC group, S. Bhadra et al., Nucl. Inst. Meth. **A 394**, 121 (1997);
ZEUS FNC Group, S. Bhadra et al., *Proc. of the Seventh International Conference on calorimetry in High Energy Physics, Tuscon, Arizona, November 1997*, E. Cheu et al. (ed.), p. 295. World Scientific, Singapore (1998).

[21] S. Bentvelsen, J. Engelen and P. Kooijman, *Proc. Workshop on Physics at HERA*, W. Buchmüller and G. Ingelman (eds.), Vol. 1, p. 23. Hamburg, Germany, DESY (1992).

[22] F. Jacquet and A. Blondel, *Proceedings of the Study for an ep Facility for Europe*, U. Amaldi (ed.), p. 391. Hamburg, Germany (1979). Also in preprint DESY 79/48.

[23] ZEUS Coll., S. Chekanov et al., Nucl. Phys. **B 627**, 3 (2002).

[24] H. Jung, Comp. Phys. Comm. **86**, 147 (1995).

[25] A. Edin, G. Ingelman and J. Rathsman, Phys. Lett. **B 366**, 371 (1996).

[26] ZEUS Coll., M. Derrick et al., Z. Phys. **C 73**, 253 (1997).

[27] T. Sjöstrand and M. Bengtsson, Comp. Phys. Comm. **43**, 367 (1987).

[28] G. Ingelman, A. Edin and J. Rathsman, Comp. Phys. Comm. **101**, 108 (1997).

[29] CTEQ Coll., H.L. Lai et al., Eur. Phys. J. **C 12**, 375 (2000).

[30] L. Lönnblad, Comp. Phys. Comm. **71**, 15 (1992).

[31] H. Jung, Comp. Phys. Comm. **143**, 100 (2002).

[32] T. Sjöstrand, Comp. Phys. Comm. **82**, 74 (1994).

[33] R. Engel, M.A. Braun, C. Pajares and J. Ranft, Z. Phys. **C 74**, 687 (1997).

[34] H1 Coll., C. Adloff et al., Z. Phys. **C 76**, 613 (1997).

[35] M. Glück, E. Reya and A. Vogt, Z. Phys. **C 53**, 651 (1992).

[36] ZEUS Coll., J. Breitweg et al., Eur. Phys. J. **C 7**, 609 (1999).

[37] ZEUS Coll., S. Chekanov et al., Nucl. Phys. **B 713**, 3 (2005).

[38] V.A. Khoze, A.D. Martin and M.G. Ryskin, Preprint IPPP-06-65, DCPT-06-130 (hep-ph/0609312), 2006.

[39] G.A. Schuler and H. Spiesberger, *Proc. Workshop on Physics at HERA*, W. Buchmüller and G. Ingelman (eds.), Vol. 3, p. 1419. Hamburg, Germany, DESY (1991).

[40] H.L. Lai et al., Phys. Rev. **D 55**, 1280 (1997).

x_L range	$\langle x_L \rangle$	$p_T^2(\,\mathrm{GeV}^2)$	$1/\sigma_{\mathrm{inc}}\, d\sigma_{\mathrm{LN}}/dx_L dp_T^2\ (\,\mathrm{GeV}^{-2})$
0.20-0.32	0.27	$7.96 \cdot 10^{-4}$	2.031 ± 0.064
		$2.51 \cdot 10^{-3}$	1.881 ± 0.064
		$4.86 \cdot 10^{-3}$	1.955 ± 0.070
		$7.95 \cdot 10^{-3}$	2.002 ± 0.068
		$1.19 \cdot 10^{-2}$	1.962 ± 0.063
		$1.65 \cdot 10^{-2}$	2.001 ± 0.062
0.32-0.42	0.37	$1.99 \cdot 10^{-3}$	1.541 ± 0.035
		$6.46 \cdot 10^{-3}$	1.454 ± 0.038
		$1.24 \cdot 10^{-2}$	1.445 ± 0.039
		$2.04 \cdot 10^{-2}$	1.527 ± 0.037
		$3.03 \cdot 10^{-2}$	1.440 ± 0.034
		$4.23 \cdot 10^{-2}$	1.256 ± 0.031
0.42-0.50	0.46	$3.42 \cdot 10^{-3}$	1.336 ± 0.026
		$1.11 \cdot 10^{-2}$	1.211 ± 0.029
		$2.14 \cdot 10^{-2}$	1.218 ± 0.029
		$3.51 \cdot 10^{-2}$	1.217 ± 0.027
		$5.22 \cdot 10^{-2}$	1.147 ± 0.025
		$7.28 \cdot 10^{-2}$	1.005 ± 0.023
0.50-0.54	0.52	$4.84 \cdot 10^{-3}$	1.274 ± 0.030
		$1.58 \cdot 10^{-2}$	1.218 ± 0.035
		$3.03 \cdot 10^{-2}$	1.200 ± 0.034
		$4.97 \cdot 10^{-2}$	1.110 ± 0.031
		$7.40 \cdot 10^{-2}$	0.946 ± 0.026
		$1.03 \cdot 10^{-1}$	0.836 ± 0.026
0.54-0.58	0.56	$5.64 \cdot 10^{-3}$	1.328 ± 0.028
		$1.84 \cdot 10^{-2}$	1.144 ± 0.031
		$3.53 \cdot 10^{-2}$	1.166 ± 0.031
		$5.80 \cdot 10^{-2}$	1.016 ± 0.027
		$8.62 \cdot 10^{-2}$	0.904 ± 0.024
		$1.20 \cdot 10^{-1}$	0.767 ± 0.023

Table 1: *The normalized doubly differential distributions* $(1/\sigma_{\mathrm{inc}})d^2\sigma_{\mathrm{LN}}/dx_L dp_T^2$ *for the full DIS sample. Only statistical uncertainties are shown.*

Table 1 (cont.)

x_L range	$\langle x_L \rangle$	p_T^2(GeV^2)	$1/\sigma_{\rm inc}\, d\sigma_{\rm LN}/dx_L dp_T^2$ (GeV^{-2})
0.58-0.62	0.60	$6.50 \cdot 10^{-3}$	1.286 ± 0.025
		$2.12 \cdot 10^{-2}$	1.175 ± 0.029
		$4.07 \cdot 10^{-2}$	1.112 ± 0.028
		$6.68 \cdot 10^{-2}$	0.976 ± 0.024
		$9.94 \cdot 10^{-2}$	0.795 ± 0.020
		$1.39 \cdot 10^{-1}$	0.654 ± 0.019
0.62-0.66	0.64	$7.42 \cdot 10^{-3}$	1.296 ± 0.024
		$2.42 \cdot 10^{-2}$	1.157 ± 0.027
		$4.65 \cdot 10^{-2}$	1.034 ± 0.025
		$7.63 \cdot 10^{-2}$	0.926 ± 0.022
		$1.14 \cdot 10^{-1}$	0.703 ± 0.018
		$1.58 \cdot 10^{-1}$	0.571 ± 0.017
0.66-0.70	0.68	$8.39 \cdot 10^{-3}$	1.297 ± 0.022
		$2.74 \cdot 10^{-2}$	1.112 ± 0.025
		$5.27 \cdot 10^{-2}$	0.990 ± 0.022
		$8.64 \cdot 10^{-2}$	0.821 ± 0.019
		$1.29 \cdot 10^{-1}$	0.581 ± 0.015
		$1.79 \cdot 10^{-1}$	0.456 ± 0.014
0.70-0.74	0.72	$9.42 \cdot 10^{-3}$	1.306 ± 0.021
		$3.08 \cdot 10^{-2}$	1.126 ± 0.023
		$5.92 \cdot 10^{-2}$	0.914 ± 0.020
		$9.71 \cdot 10^{-2}$	0.707 ± 0.016
		$1.44 \cdot 10^{-1}$	0.524 ± 0.013
		$2.01 \cdot 10^{-1}$	0.388 ± 0.012
0.74-0.78	0.76	$1.05 \cdot 10^{-2}$	1.280 ± 0.019
		$3.44 \cdot 10^{-2}$	1.030 ± 0.021
		$6.61 \cdot 10^{-2}$	0.837 ± 0.018
		$1.08 \cdot 10^{-1}$	0.617 ± 0.014
		$1.61 \cdot 10^{-1}$	0.403 ± 0.011
		$2.25 \cdot 10^{-1}$	0.308 ± 0.010

Table 1 (cont.)

x_L range	$\langle x_L \rangle$	p_T^2(GeV^2)	$1/\sigma_{\rm inc}\ d\sigma_{\rm LN}/dx_L dp_T^2$ (GeV^{-2})
0.78-0.82	0.80	$1.16 \cdot 10^{-2}$	1.180 ± 0.018
		$3.81 \cdot 10^{-2}$	0.920 ± 0.019
		$7.33 \cdot 10^{-2}$	0.714 ± 0.016
		$1.20 \cdot 10^{-1}$	0.482 ± 0.012
		$1.79 \cdot 10^{-1}$	0.304 ± 0.009
		$2.49 \cdot 10^{-1}$	0.213 ± 0.008
0.82-0.86	0.84	$1.28 \cdot 10^{-2}$	1.000 ± 0.016
		$4.21 \cdot 10^{-2}$	0.783 ± 0.017
		$8.10 \cdot 10^{-2}$	0.568 ± 0.014
		$1.33 \cdot 10^{-1}$	0.374 ± 0.010
		$1.98 \cdot 10^{-1}$	0.208 ± 0.007
		$2.75 \cdot 10^{-1}$	0.139 ± 0.006
0.86-0.90	0.88	$1.41 \cdot 10^{-2}$	0.719 ± 0.013
		$4.63 \cdot 10^{-2}$	0.537 ± 0.013
		$8.90 \cdot 10^{-2}$	0.363 ± 0.010
		$1.46 \cdot 10^{-1}$	0.232 ± 0.007
		$2.17 \cdot 10^{-1}$	0.135 ± 0.005
		$3.03 \cdot 10^{-1}$	0.082 ± 0.004
0.90-0.95	0.92	$1.54 \cdot 10^{-2}$	0.347 ± 0.007
		$5.07 \cdot 10^{-2}$	0.267 ± 0.008
		$9.74 \cdot 10^{-2}$	0.172 ± 0.006
		$1.60 \cdot 10^{-1}$	0.110 ± 0.004
		$2.38 \cdot 10^{-1}$	0.059 ± 0.003
		$3.31 \cdot 10^{-1}$	0.034 ± 0.002
0.95-1.00	0.97	$1.72 \cdot 10^{-2}$	0.054 ± 0.002
		$5.64 \cdot 10^{-2}$	0.043 ± 0.002
		$1.08 \cdot 10^{-1}$	0.032 ± 0.002
		$1.78 \cdot 10^{-1}$	0.015 ± 0.001
		$2.65 \cdot 10^{-1}$	0.009 ± 0.001
		$3.69 \cdot 10^{-1}$	0.005 ± 0.001

x_L range	$\langle x_L \rangle$	$a\,(\text{GeV}^{-2})$	$b\,(\text{GeV}^{-2})$
0.20-0.32	0.27	$1.958 \pm 0.045^{+0.19}_{-0.14}$	$-0.94 \pm 2.40^{+2.19}_{-1.16}$
0.32-0.42	0.37	$1.551 \pm 0.025^{+0.10}_{-0.08}$	$3.93 \pm 0.68^{+0.66}_{-0.90}$
0.42-0.50	0.46	$1.325 \pm 0.020^{+0.10}_{-0.07}$	$3.38 \pm 0.37^{+0.67}_{-0.54}$
0.50-0.54	0.52	$1.324 \pm 0.024^{+0.12}_{-0.09}$	$4.32 \pm 0.33^{+0.68}_{-0.53}$
0.54-0.58	0.56	$1.327 \pm 0.022^{+0.10}_{-0.08}$	$4.53 \pm 0.27^{+0.45}_{-0.28}$
0.58-0.62	0.60	$1.336 \pm 0.021^{+0.14}_{-0.10}$	$5.09 \pm 0.22^{+0.55}_{-0.60}$
0.62-0.66	0.64	$1.343 \pm 0.020^{+0.16}_{-0.08}$	$5.44 \pm 0.19^{+0.82}_{-0.30}$
0.66-0.70	0.68	$1.357 \pm 0.019^{+0.11}_{-0.07}$	$6.23 \pm 0.17^{+0.50}_{-0.45}$
0.70-0.74	0.72	$1.370 \pm 0.018^{+0.15}_{-0.12}$	$6.53 \pm 0.15^{+0.72}_{-0.58}$
0.74-0.78	0.76	$1.344 \pm 0.017^{+0.08}_{-0.07}$	$7.06 \pm 0.14^{+0.59}_{-0.61}$
0.78-0.82	0.80	$1.258 \pm 0.017^{+0.09}_{-0.04}$	$7.66 \pm 0.14^{+0.73}_{-0.57}$
0.82-0.86	0.84	$1.098 \pm 0.015^{+0.05}_{-0.07}$	$8.04 \pm 0.14^{+0.65}_{-0.54}$
0.86-0.90	0.88	$0.782 \pm 0.013^{+0.09}_{-0.13}$	$8.03 \pm 0.15^{+0.46}_{-0.45}$
0.90-0.95	0.92	$0.387 \pm 0.007^{+0.12}_{-0.12}$	$7.79 \pm 0.17^{+0.60}_{-0.45}$
0.95-1.00	0.97	$0.063 \pm 0.002^{+0.05}_{-0.04}$	$7.46 \pm 0.28^{+0.59}_{-0.47}$

Table 2: *The intercepts a and slopes b from the exponential parameterization of the differential cross defined in Section 4.1 for the full DIS sample. Statistical uncertainties are listed first, followed by systematic uncertainties, not including an overall normalization uncertainty of 2.1% on the intercepts. The systematic uncertainties are largely correlated between all points.*

sample	Q^2 range (GeV^2)	$\langle Q^2 \rangle$ (GeV^2)	W range (GeV)	$\langle W \rangle$ (GeV)
γp	$Q^2 < 0.02$	4×10^{-4}	$150 < W < 270$	215
full DIS	$Q^2 > 2$	13	$W < 250$	95
low-Q^2 DIS	$2 < Q^2_{DA} < 5$	2.7	$50 < W < 250$	140
mid-Q^2 DIS	$5 < Q^2_{DA} < 20$	8.9	$50 < W < 250$	132
high-Q^2 DIS	$20 < Q^2_{DA} < 120$	40	$50 < W < 250$	131

Table 3: *Kinematic regions for each of the data samples. The γp ranges were estimated from a simulation of photoproduction including the positron tagger used to trigger these data. The Q^2 ranges for the low-, mid-, and high-Q^2 DIS samples are the limits on the double angle variable Q^2_{DA}. All other ranges and means for DIS were estimated using the DJANGOH 1.1 [39] generator, where the CTEQ4D [40] parton-density parameterizations were used.*

sample	$r_{\rm LN}$
γp	$0.0700 \pm 0.0004\ ^{+0.0040}_{-0.0040}$
full DIS	$0.0885 \pm 0.0002\ ^{+0.0029}_{-0.0022}$
low-Q^2 DIS	$0.0837 \pm 0.0003\ ^{+0.0020}_{-0.0020}$
mid-Q^2 DIS	$0.0843 \pm 0.0003\ ^{+0.0020}_{-0.0019}$
high-Q^2 DIS	$0.0913 \pm 0.0006\ ^{+0.0021}_{-0.0021}$

Table 4: *$r_{\rm LN}$ in the region $x_L > 0.2, p_T^2 < 0.476 x_L^2$ GeV^2, for the photoproduction and DIS samples. Statistical uncertainties are listed first, followed by systematic uncertainties, not including an overall normalization uncertainty of 2.1%.*

			$1/\sigma_{\rm inc}\, d\sigma_{\rm LN}/dx_L dp_T^2$ (GeV^{-2})			
x_L range	$\langle x_L \rangle$	p_T^2(GeV^2)	γp	low-Q^2 DIS	mid-Q^2 DIS	high-Q^2 DIS
0.20-0.50	0.38	$8.40 \cdot 10^{-4}$	1.501 ± 0.108	1.491 ± 0.058	1.721 ± 0.063	1.848 ± 0.115
		$2.43 \cdot 10^{-3}$	1.289 ± 0.090	1.342 ± 0.052	1.500 ± 0.056	1.749 ± 0.106
		$4.86 \cdot 10^{-3}$	1.127 ± 0.076	1.370 ± 0.052	1.451 ± 0.053	1.757 ± 0.104
		$7.94 \cdot 10^{-3}$	1.232 ± 0.084	1.417 ± 0.054	1.528 ± 0.057	1.809 ± 0.110
		$1.19 \cdot 10^{-2}$	1.064 ± 0.075	1.359 ± 0.053	1.451 ± 0.055	1.803 ± 0.109
		$1.65 \cdot 10^{-2}$	1.021 ± 0.068	1.374 ± 0.052	1.589 ± 0.056	1.805 ± 0.106
0.50-0.58	0.54	$4.84 \cdot 10^{-3}$	0.988 ± 0.056	1.196 ± 0.036	1.247 ± 0.037	1.452 ± 0.071
		$1.58 \cdot 10^{-2}$	0.791 ± 0.055	1.077 ± 0.042	1.096 ± 0.042	1.220 ± 0.079
		$3.03 \cdot 10^{-2}$	0.812 ± 0.058	1.027 ± 0.040	1.042 ± 0.041	1.191 ± 0.078
		$4.97 \cdot 10^{-2}$	0.784 ± 0.052	1.005 ± 0.037	1.009 ± 0.037	1.187 ± 0.072
		$7.39 \cdot 10^{-2}$	0.654 ± 0.043	0.880 ± 0.033	0.857 ± 0.032	0.934 ± 0.060
		$1.03 \cdot 10^{-1}$	0.591 ± 0.041	0.768 ± 0.031	0.760 ± 0.031	0.782 ± 0.056
0.58-0.66	0.62	$6.50 \cdot 10^{-3}$	0.991 ± 0.047	1.192 ± 0.031	1.261 ± 0.032	1.221 ± 0.055
		$2.12 \cdot 10^{-2}$	0.849 ± 0.051	1.062 ± 0.035	1.122 ± 0.037	1.131 ± 0.065
		$4.08 \cdot 10^{-2}$	0.892 ± 0.055	1.025 ± 0.034	1.068 ± 0.035	1.151 ± 0.065
		$6.68 \cdot 10^{-2}$	0.753 ± 0.045	0.906 ± 0.030	0.889 ± 0.030	1.090 ± 0.059
		$9.94 \cdot 10^{-2}$	0.563 ± 0.035	0.714 ± 0.025	0.748 ± 0.025	0.837 ± 0.048
		$1.39 \cdot 10^{-1}$	0.451 ± 0.031	0.575 ± 0.023	0.605 ± 0.023	0.626 ± 0.042
0.66-0.74	0.70	$8.38 \cdot 10^{-3}$	1.083 ± 0.044	1.303 ± 0.028	1.263 ± 0.028	1.309 ± 0.050
		$2.74 \cdot 10^{-2}$	0.882 ± 0.047	1.116 ± 0.032	1.093 ± 0.031	1.104 ± 0.056
		$5.27 \cdot 10^{-2}$	0.815 ± 0.045	0.935 ± 0.028	0.961 ± 0.029	1.035 ± 0.054
		$8.64 \cdot 10^{-2}$	0.688 ± 0.039	0.751 ± 0.024	0.739 ± 0.023	0.745 ± 0.042
		$1.28 \cdot 10^{-1}$	0.451 ± 0.027	0.530 ± 0.018	0.560 ± 0.019	0.532 ± 0.033
		$1.79 \cdot 10^{-1}$	0.305 ± 0.021	0.426 ± 0.017	0.428 ± 0.017	0.448 ± 0.031

Table 5: *The normalized doubly differential distributions* $(1/\sigma_{\rm inc}) d^2\sigma_{\rm LN}/dx_L dp_T^2$ *for the photoproduction and three DIS samples. Only statistical uncertainties are shown.*

Table 5 (cont.)

			$1/\sigma_{\rm inc}\, d\sigma_{\rm LN}/dx_L dp_T^2$ (GeV^{-2})			
x_L range	$\langle x_L \rangle$	p_T^2(GeV^2)	γp	low-Q^2 DIS	mid-Q^2 DIS	high-Q^2 DIS
0.74-0.82	0.78	$1.05 \cdot 10^{-2}$	1.111 ± 0.041	1.250 ± 0.025	1.181 ± 0.024	1.251 ± 0.044
		$3.44 \cdot 10^{-2}$	0.884 ± 0.043	1.027 ± 0.027	0.986 ± 0.027	0.915 ± 0.046
		$6.61 \cdot 10^{-2}$	0.769 ± 0.042	0.824 ± 0.024	0.779 ± 0.023	0.846 ± 0.043
		$1.08 \cdot 10^{-1}$	0.494 ± 0.028	0.587 ± 0.018	0.541 ± 0.018	0.576 ± 0.033
		$1.61 \cdot 10^{-1}$	0.285 ± 0.018	0.361 ± 0.013	0.362 ± 0.013	0.399 ± 0.025
		$2.25 \cdot 10^{-1}$	0.209 ± 0.016	0.267 ± 0.012	0.243 ± 0.011	0.289 ± 0.022
0.82-0.90	0.86	$1.28 \cdot 10^{-2}$	0.876 ± 0.034	0.899 ± 0.019	0.894 ± 0.019	0.838 ± 0.032
		$4.21 \cdot 10^{-2}$	0.688 ± 0.036	0.732 ± 0.021	0.671 ± 0.020	0.647 ± 0.035
		$8.09 \cdot 10^{-2}$	0.538 ± 0.033	0.528 ± 0.017	0.477 ± 0.016	0.477 ± 0.029
		$1.33 \cdot 10^{-1}$	0.293 ± 0.020	0.335 ± 0.013	0.329 ± 0.012	0.268 ± 0.020
		$1.97 \cdot 10^{-1}$	0.134 ± 0.011	0.195 ± 0.009	0.170 ± 0.008	0.174 ± 0.015
		$2.75 \cdot 10^{-1}$	0.098 ± 0.010	0.116 ± 0.007	0.113 ± 0.007	0.116 ± 0.012
0.90-1.00	0.93	$1.54 \cdot 10^{-2}$	0.242 ± 0.015	0.236 ± 0.008	0.228 ± 0.007	0.201 ± 0.012
		$5.06 \cdot 10^{-2}$	0.166 ± 0.014	0.180 ± 0.008	0.156 ± 0.007	0.142 ± 0.013
		$9.74 \cdot 10^{-2}$	0.130 ± 0.012	0.117 ± 0.006	0.115 ± 0.006	0.093 ± 0.010
		$1.60 \cdot 10^{-1}$	0.072 ± 0.008	0.077 ± 0.005	0.065 ± 0.004	0.057 ± 0.007
		$2.38 \cdot 10^{-1}$	0.039 ± 0.005	0.041 ± 0.003	0.035 ± 0.003	0.034 ± 0.005
		$3.31 \cdot 10^{-1}$	0.022 ± 0.004	0.019 ± 0.002	0.023 ± 0.002	0.019 ± 0.004

sample	x_L range	$\langle x_L \rangle$	a (GeV^{-2})	b (GeV^{-2})
γp	0.20-0.50	0.38	$1.386 \pm 0.068^{+0.10}_{-0.10}$	$20.32 \pm 5.27^{+1.68}_{-2.44}$
	0.50-0.58	0.54	$0.949 \pm 0.041^{+0.07}_{-0.10}$	$4.72 \pm 0.78^{+0.73}_{-0.68}$
	0.58-0.66	0.62	$1.037 \pm 0.039^{+0.13}_{-0.08}$	$5.82 \pm 0.53^{+0.76}_{-0.65}$
	0.66-0.74	0.70	$1.149 \pm 0.038^{+0.11}_{-0.11}$	$7.13 \pm 0.40^{+0.70}_{-0.78}$
	0.74-0.82	0.78	$1.217 \pm 0.038^{+0.10}_{-0.05}$	$8.32 \pm 0.33^{+0.75}_{-0.55}$
	0.82-0.90	0.86	$1.009 \pm 0.035^{+0.04}_{-0.09}$	$9.23 \pm 0.33^{+0.50}_{-0.64}$
	0.90-1.00	0.93	$0.266 \pm 0.014^{+0.09}_{-0.10}$	$7.91 \pm 0.44^{+0.64}_{-0.41}$
low-Q^2 DIS	0.20-0.50	0.38	$1.412 \pm 0.038^{+0.10}_{-0.09}$	$2.21 \pm 2.92^{+2.17}_{-2.18}$
	0.50-0.58	0.54	$1.196 \pm 0.029^{+0.07}_{-0.07}$	$4.20 \pm 0.44^{+0.51}_{-0.40}$
	0.58-0.66	0.62	$1.238 \pm 0.025^{+0.13}_{-0.09}$	$5.40 \pm 0.30^{+0.95}_{-0.70}$
	0.66-0.74	0.70	$1.359 \pm 0.025^{+0.09}_{-0.13}$	$6.88 \pm 0.23^{+0.42}_{-0.73}$
	0.74-0.82	0.78	$1.346 \pm 0.023^{+0.05}_{-0.06}$	$7.65 \pm 0.19^{+0.49}_{-0.74}$
	0.82-0.90	0.86	$1.005 \pm 0.019^{+0.06}_{-0.10}$	$8.10 \pm 0.18^{+0.47}_{-0.53}$
	0.90-1.00	0.93	$0.266 \pm 0.008^{+0.10}_{-0.08}$	$7.94 \pm 0.25^{+0.41}_{-0.55}$
mid-Q^2 DIS	0.20-0.50	0.38	$1.552 \pm 0.041^{+0.12}_{-0.08}$	$1.80 \pm 2.87^{+2.87}_{-2.18}$
	0.50-0.58	0.54	$1.238 \pm 0.029^{+0.10}_{-0.09}$	$4.80 \pm 0.44^{+0.51}_{-0.47}$
	0.58-0.66	0.62	$1.298 \pm 0.026^{+0.10}_{-0.10}$	$5.53 \pm 0.30^{+0.54}_{-0.42}$
	0.66-0.74	0.70	$1.324 \pm 0.024^{+0.09}_{-0.10}$	$6.51 \pm 0.22^{+0.61}_{-0.49}$
	0.74-0.82	0.78	$1.276 \pm 0.022^{+0.07}_{-0.07}$	$7.65 \pm 0.19^{+0.57}_{-0.58}$
	0.82-0.90	0.86	$0.975 \pm 0.019^{+0.05}_{-0.08}$	$8.40 \pm 0.19^{+0.54}_{-0.54}$
	0.90-1.00	0.93	$0.248 \pm 0.008^{+0.10}_{-0.09}$	$7.99 \pm 0.28^{+0.45}_{-0.54}$
high-Q^2 DIS	0.20-0.50	0.38	$1.786 \pm 0.076^{+0.13}_{-0.15}$	$-0.53 \pm 4.56^{+4.71}_{-2.92}$
	0.50-0.58	0.54	$1.449 \pm 0.056^{+0.05}_{-0.10}$	$5.79 \pm 0.74^{+0.61}_{-0.78}$
	0.58-0.66	0.62	$1.309 \pm 0.045^{+0.15}_{-0.11}$	$4.66 \pm 0.48^{+0.92}_{-0.69}$
	0.66-0.74	0.70	$1.374 \pm 0.044^{+0.11}_{-0.05}$	$6.76 \pm 0.40^{+0.55}_{-0.63}$
	0.74-0.82	0.78	$1.283 \pm 0.039^{+0.03}_{-0.07}$	$7.02 \pm 0.33^{+0.78}_{-0.58}$
	0.82-0.90	0.86	$0.915 \pm 0.032^{+0.05}_{-0.09}$	$8.29 \pm 0.36^{+0.61}_{-0.71}$
	0.90-1.00	0.93	$0.217 \pm 0.013^{+0.10}_{-0.08}$	$7.93 \pm 0.53^{+0.38}_{-0.53}$

Table 6: *The intercepts a and slopes b from the exponential parameterization of the differential cross defined in Section 4.1 for the photoproduction and three DIS samples. Statistical uncertainties are listed first, followed by systematic uncertainties, not including an overall normalization uncertainty of 2.1% on the intercepts in DIS, nor an additional uncorrelated uncertainty of 5.1% on the photoproduction intercepts. The systematic uncertainties are largely correlated between all points.*

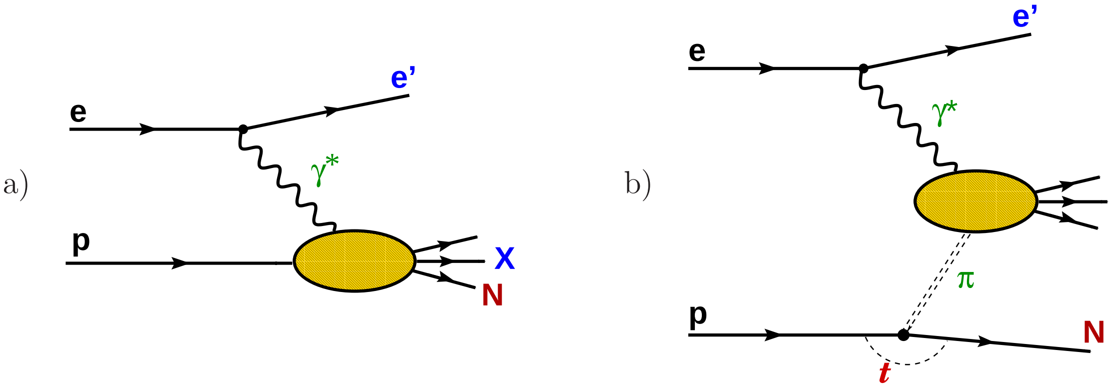

Figure 1: *a) HERA ep scattering event with the final-state baryon in the proton-fragmentation system, X. b) Leading baryon production via an exchange process.*

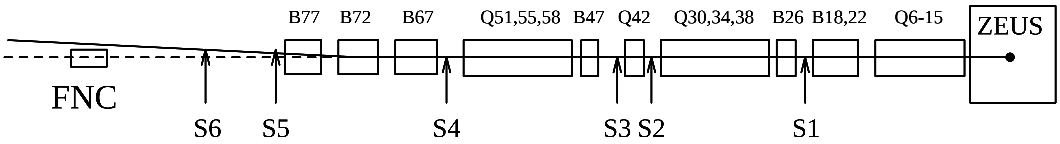

Figure 2: *Side view of the proton beamline downstream from the ZEUS interaction region. The protons are moving from right to left. The labels for the HERA components, e.g. B47, indicate the horizontal distance in meters from the interaction point. The horizontal and vertical axes are not to scale. The proton beam is bent upward by approximately 6 mrad by the dipole magnets B67–B77 near Z=+70 m. The FNC is located on the zero-degree line at Z=+105.5 m. S1–S6 indicate the locations of the ZEUS leading-proton spectrometer stations [26].*

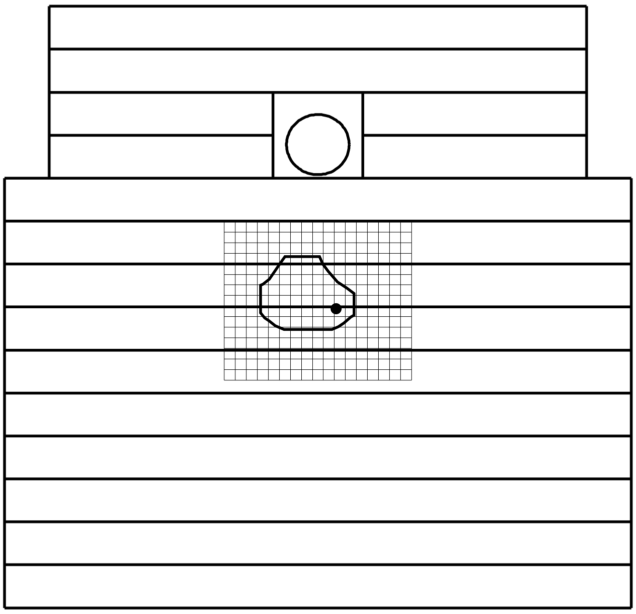

Figure 3: *Diagram of the FNC/FNT assembly. The thick horizontal lines show the 5 cm vertical segmentation of the front part of the FNC. The hole through the third and fourth towers from the top allows the proton beam to pass through the calorimeter. The 17×15 grid of small squares shows the fingers of the FNT hodoscopes. The irregular curve shows the geometric aperture defined by upstream beamline elements, and the bullet (●) shows the zero-degree point.*

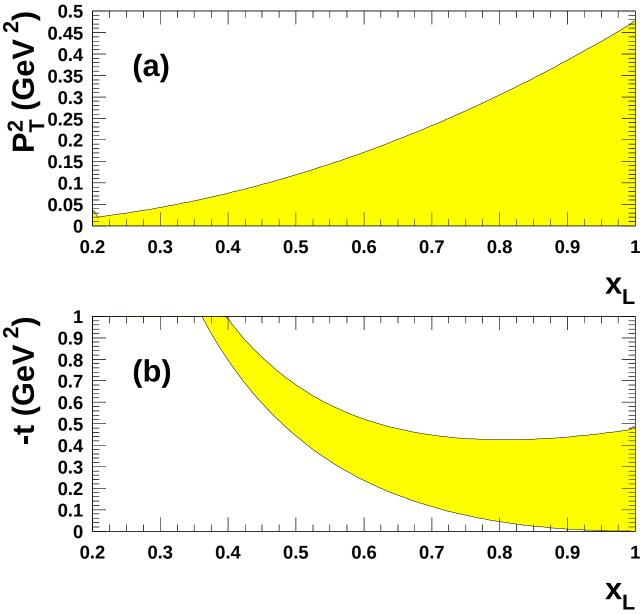

Figure 4: *The kinematic regions in (a) p_T^2 and (b) t covered by the angular acceptance of the FNC ($\theta_n < 0.75\,mrad$) are shown as shaded bands.*

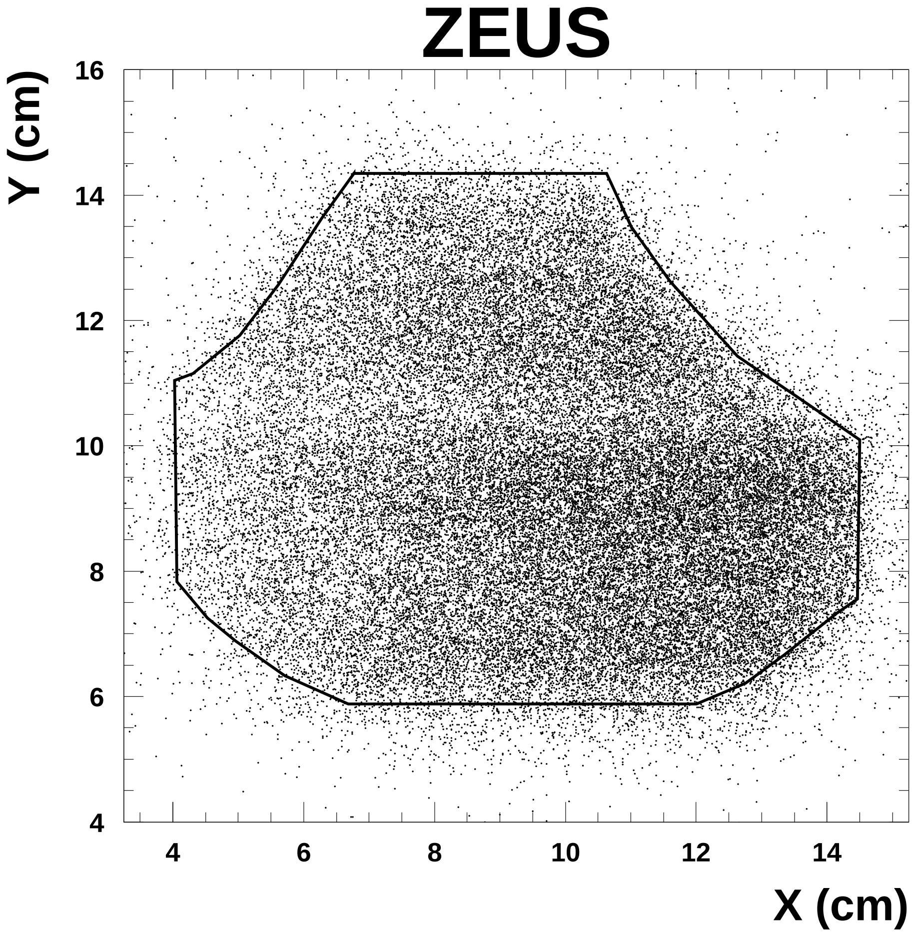

Figure 5: *Scatter plot of reconstructed positions in the FNT. The irregular curve is the geometric aperture defined by upstream beamline elements as modeled in the Monte Carlo. The zero-degree point is at* $X = 12.5\,cm$*,* $Y = 8.3\,cm$*. The deficit of events observed near* $Y \sim 10.5\,cm$ *is due to dead material in the LPS.*

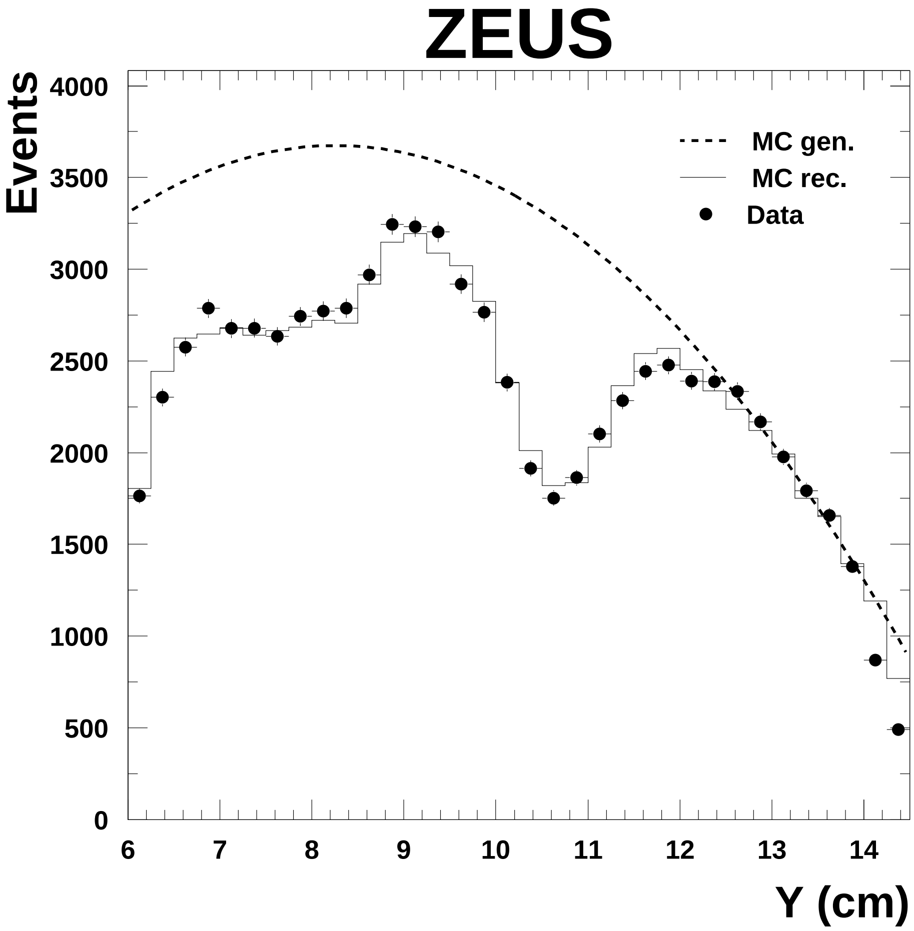

Figure 6: *Vertical slice of the data in Fig. 5 for* $7 < X < 10.5$ *cm. The smooth curve is the generated Monte Carlo distribution; the histogram is the Monte Carlo distribution of reconstructed events after the dead material simulation. The peak of the smooth curve, determined from a fit to the data, corresponds to the zero-degree point in the vertical plane.*

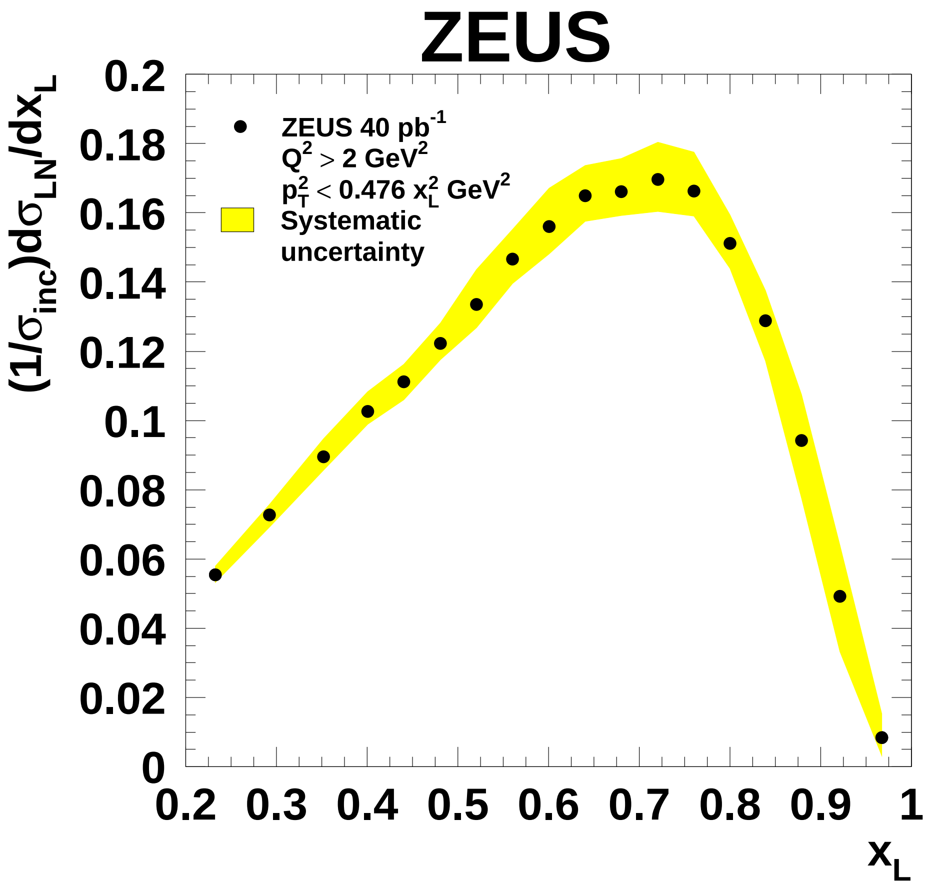

Figure 7: *The distribution* $(1/\sigma_{\rm inc})d\sigma_{\rm LN}/dx_L$ *for neutrons in DIS with scattering angles* $\theta_n < 0.75$ *mrad, corresponding to the kinematic range* $p_T^2 < 0.476\,x_L^2$ *GeV*^{2}*. The statistical uncertainties are smaller than the plotted symbols; the shaded band shows the systematic uncertainties. The band does not include the overall normalization uncertainty of* 2.1%*.*

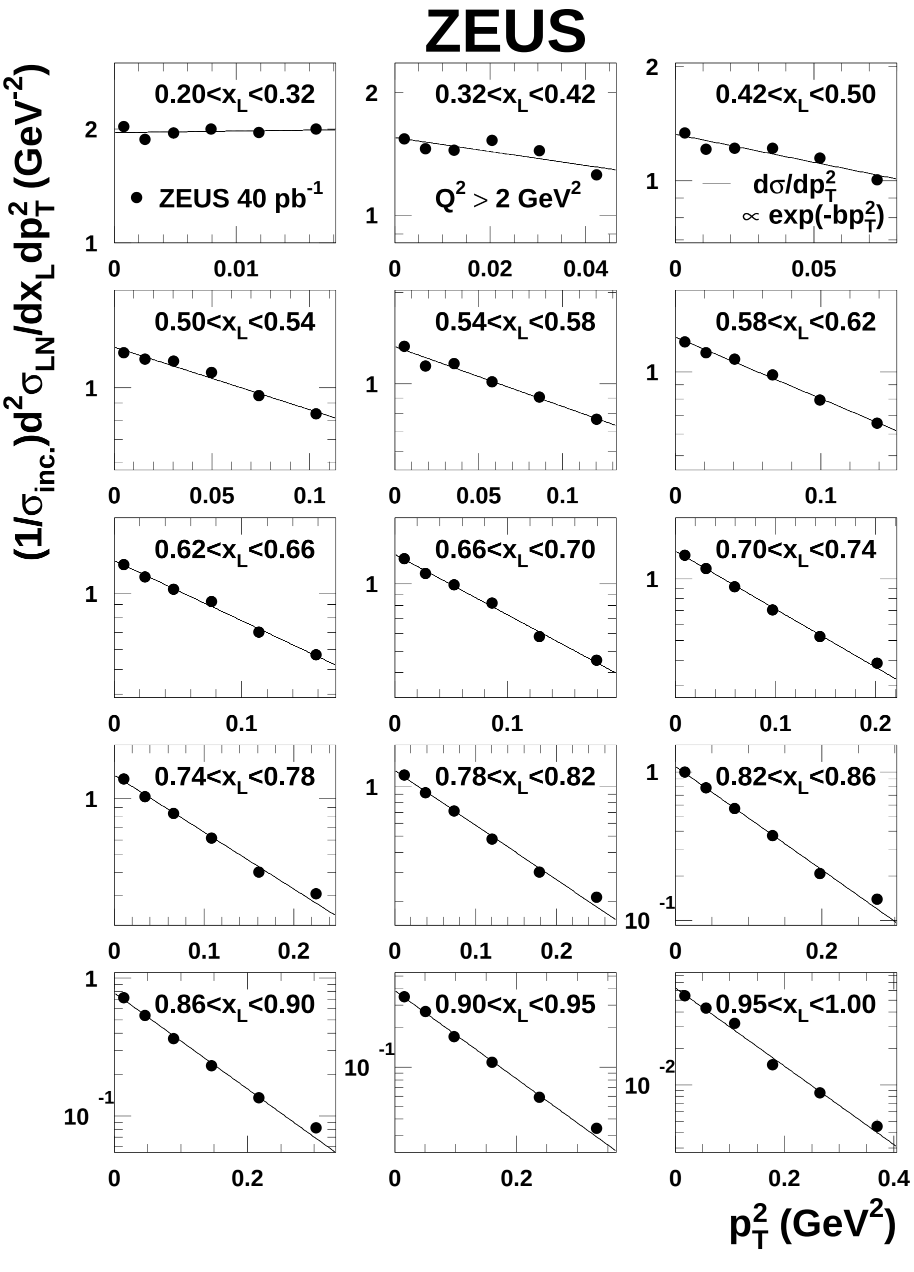

Figure 8: *The* p_T^2 *distributions for DIS. Note the logarithmic vertical scale and the varying* p_T^2 *ranges. The statistical uncertainties are shown by a vertical error bar; in most cases they are smaller than the plotted symbol. The systematic uncertainties are not shown. The line on each plot is the result of a fit to the form* $d\sigma_{\mathrm{LN}}/dp_T^2 \propto \exp(-bp_T^2)$.

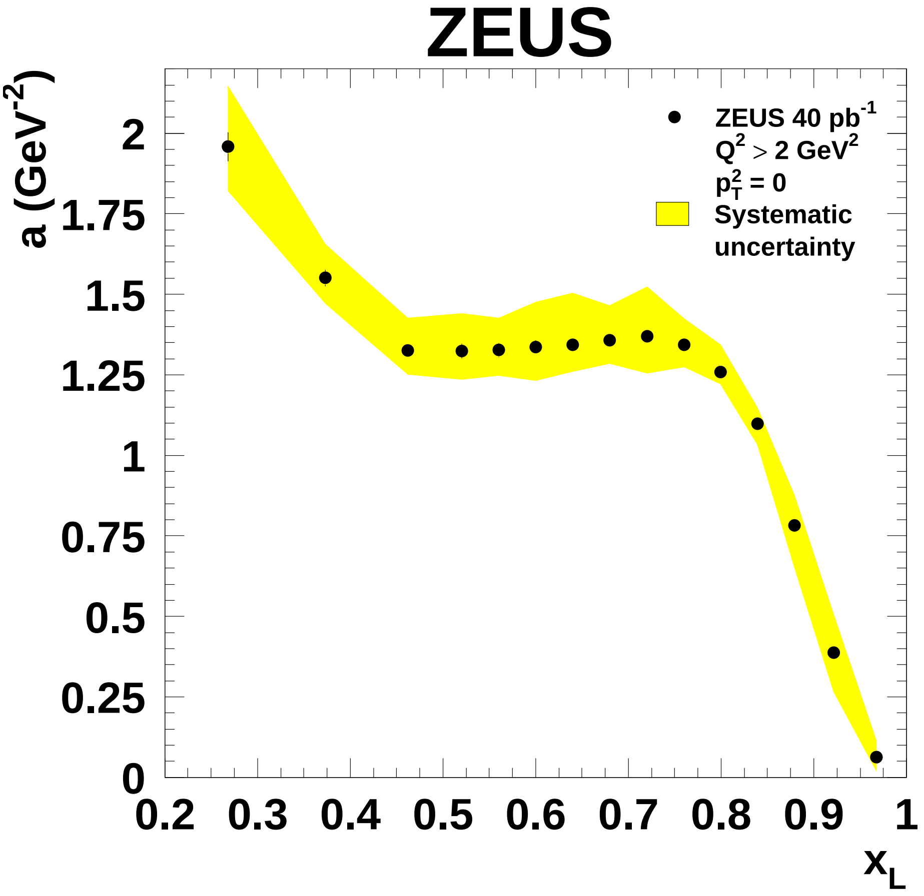

Figure 9: *The intercepts* $a = (1/\sigma_{\rm inc}) d^2\sigma_{\rm LN}/dx_L dp_T^2|_{p_T^2=0}$ *versus* x_L *from fits of the* p_T^2 *distributions in DIS to the form* $d\sigma_{\rm LN}/dp_T^2 = a\exp(-bp_T^2)$ *over the* p_T^2 *ranges shown in Fig. 8. The statistical uncertainties are shown by a vertical error bar; in most cases they are smaller than the plotted symbol. The shaded band shows the systematic uncertainties. The band does not include the overall normalization uncertainty of* 2.1%*.*

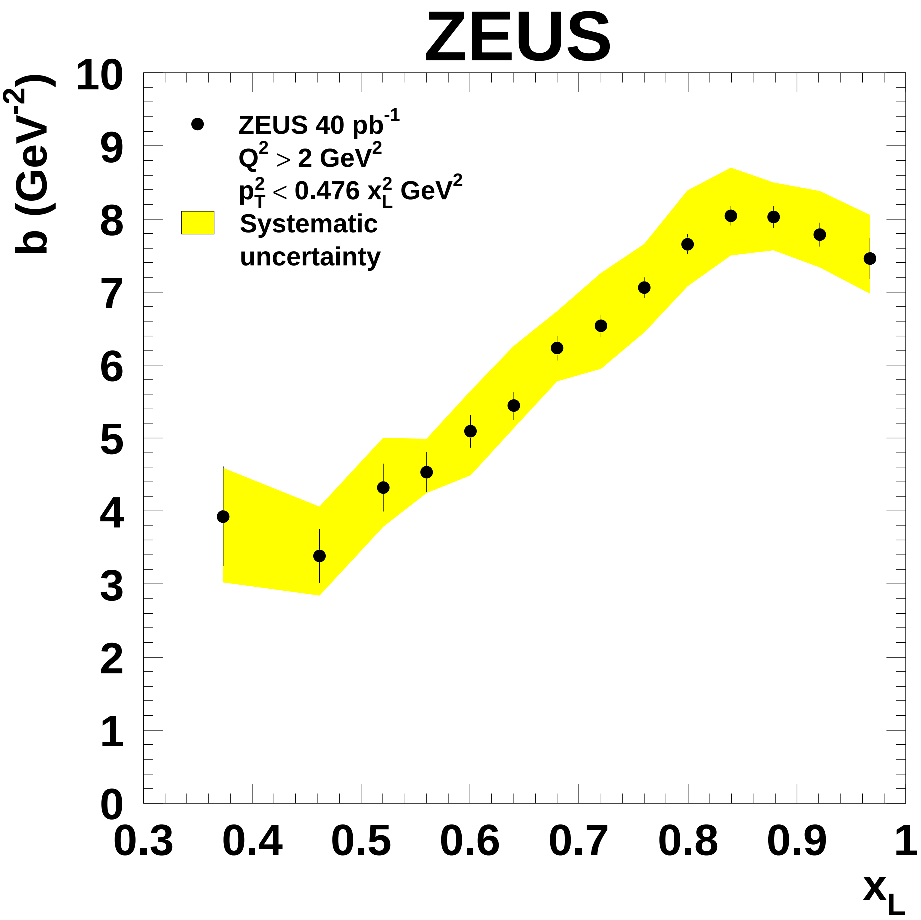

Figure 10: *The exponential slopes b versus x_L from fits of the p_T^2 distributions in DIS to the form $d\sigma_{\rm LN}/dp_T^2 = a\exp(-bp_T^2)$ over the p_T^2 ranges shown in Fig. 8. The error bars show the statistical uncertainties; the shaded band shows the systematic uncertainties.*

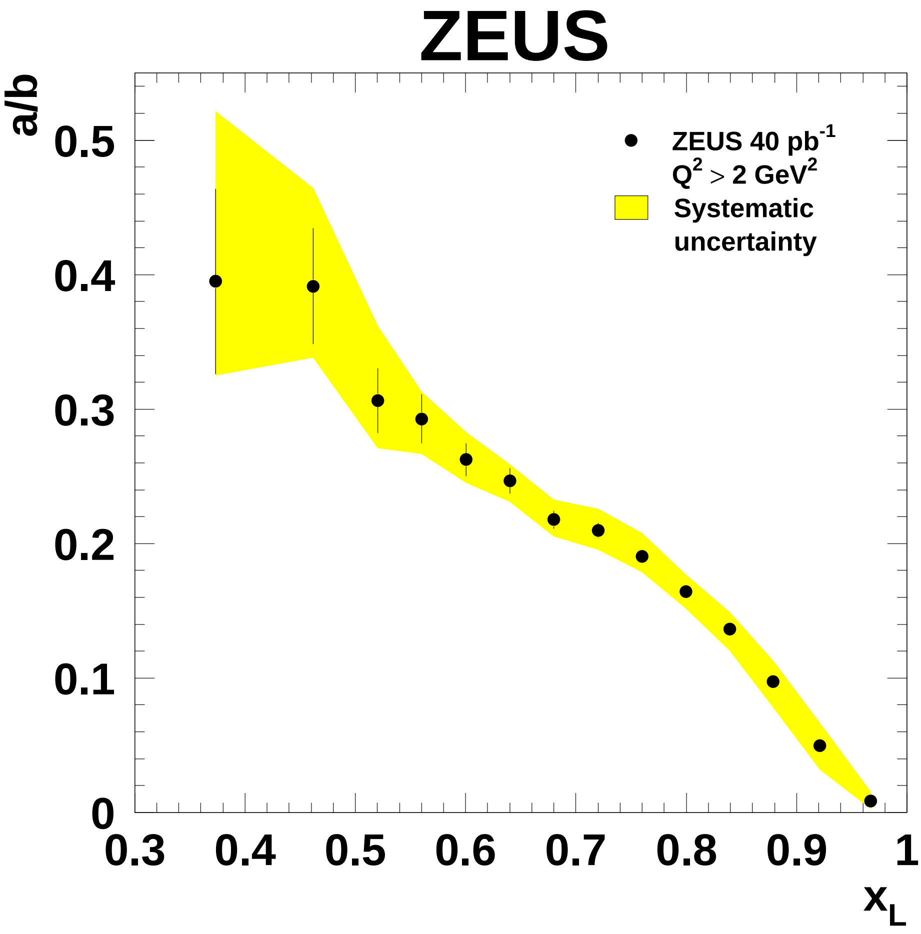

Figure 11: *The ratio a/b versus x_L from fits of the p_T^2 distributions in DIS to the form $d\sigma_{\rm LN}/dp_T^2 = a\exp(-bp_T^2)$ over the p_T^2 ranges shown in Fig. 8. The error bars show the statistical uncertainties; the shaded band shows the systematic uncertainties. The band does not include the overall normalization uncertainty of 2.1%.*

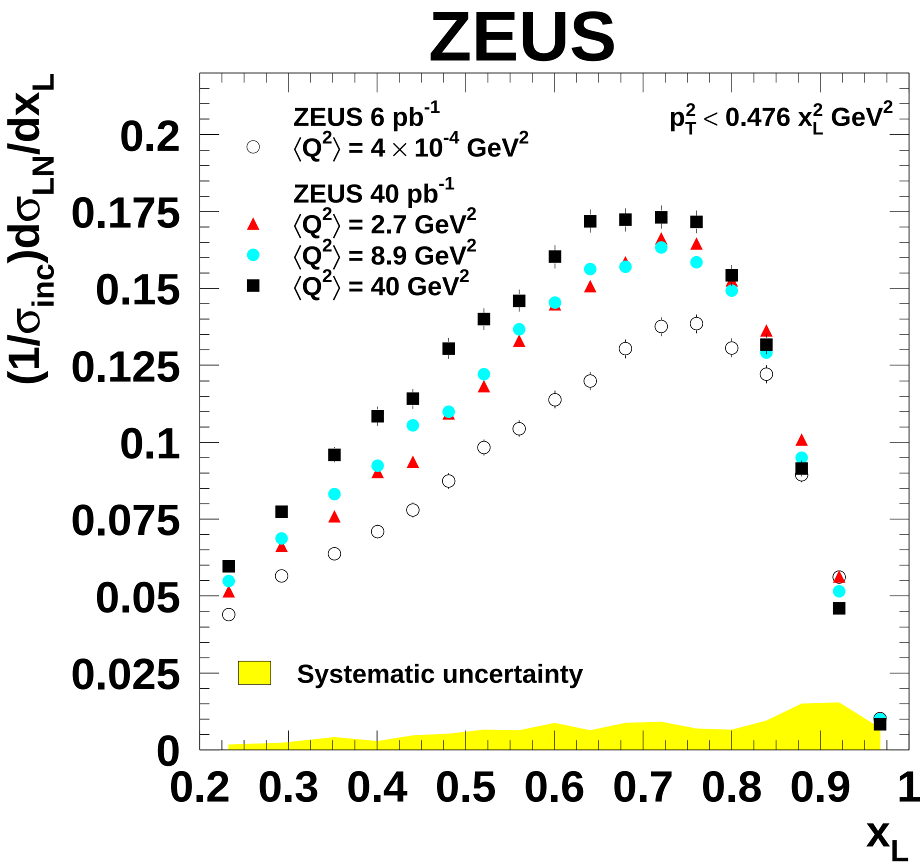

Figure 12: *The x_L distributions for the photoproduction and three DIS subsamples. The error bars show the statistical uncertainties. The common systematic uncertainties are shown as a shaded band. There is an overall normalization uncertainty of* 2.1% *for the DIS data, and an additional uncorrelated uncertainty of* 5.1% *for the photoproduction data.*

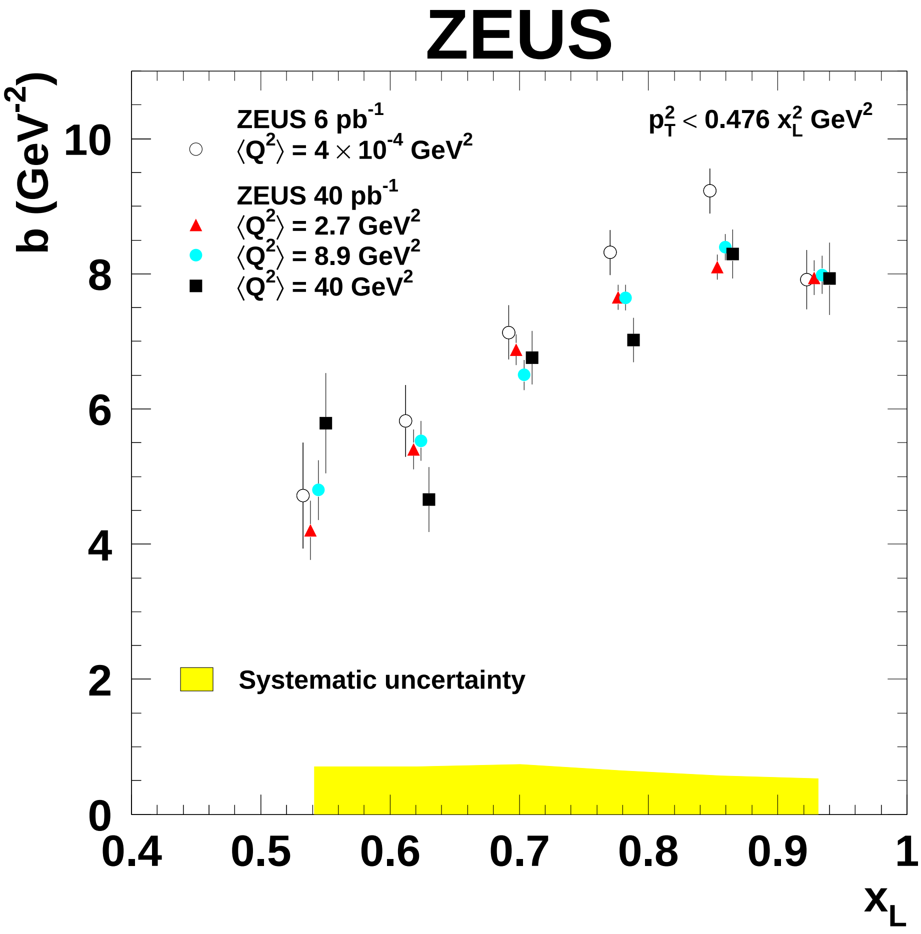

Figure 13: *The exponential slopes b for the photoproduction and three DIS subsamples. The points are slightly offset horizontally for clarity. The error bars show the statistical uncertainties. The common systematic uncertainties are shown as a shaded band.*

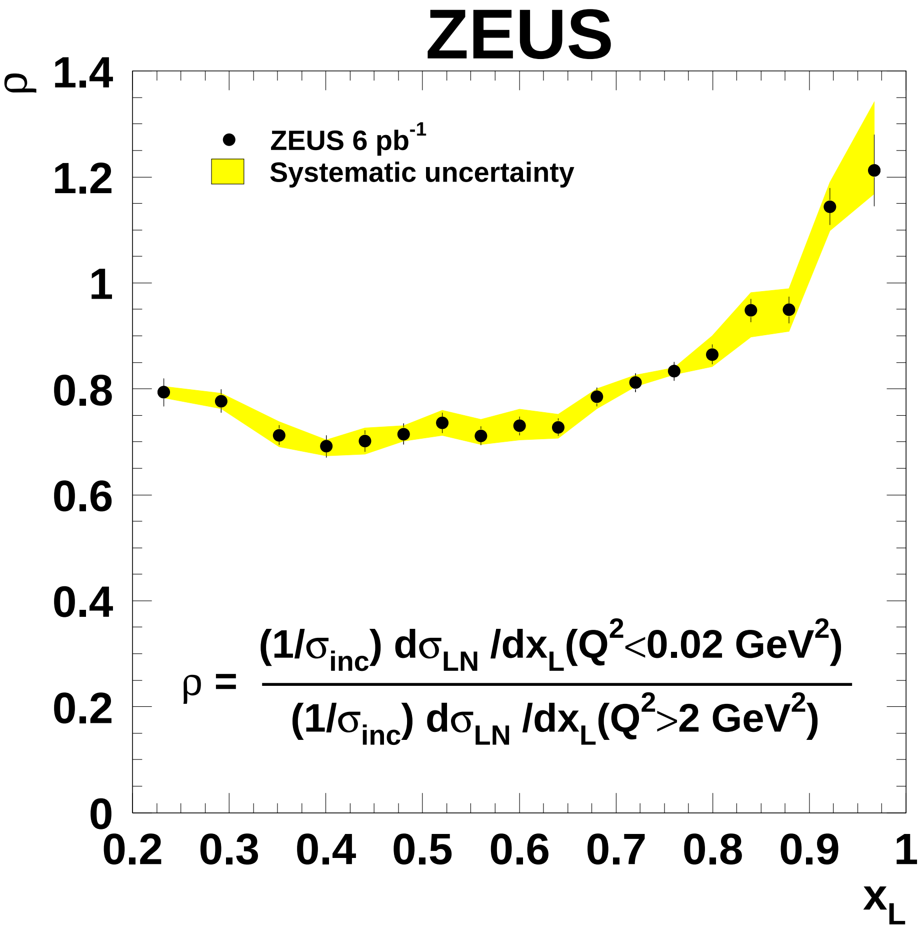

Figure 14: *The ratio of the* x_L *distributions for photoproduction and DIS, normalized as described in the text, for neutrons with scattering angles* $\theta_n < 0.75$ *mrad, corresponding to the kinematic range* $p_T^2 < 0.476\, x_L^2$ *GeV*^{2}*. The error bars show the statistical uncertainties; the shaded band shows the systematic uncertainties. The band does not include the overall normalization uncertainty of* 5.1% *on the ratio.*

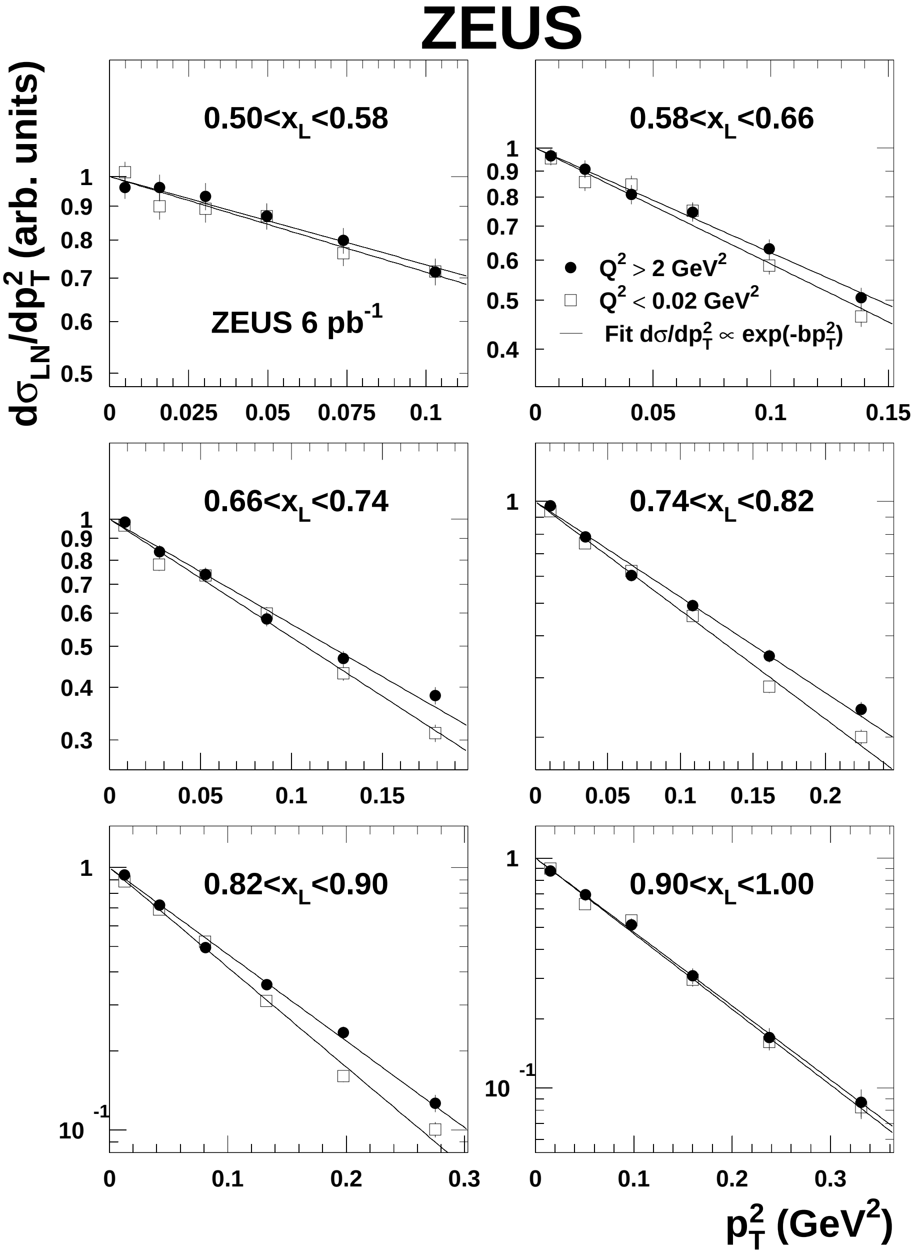

Figure 15: *The p_T^2 distributions for photoproduction and DIS. They are each normalized to unity at $p_T^2 = 0$. Note the logarithmic vertical scale and the varying p_T^2 ranges. The statistical uncertainties are shown by a vertical error bar; in some cases they are smaller than the plotted symbol. The systematic uncertainties are not shown. The lines on each plot are the results of fits to the form* $d\sigma_{\rm LN}/dp_T^2 \propto \exp(-bp_T^2)$.

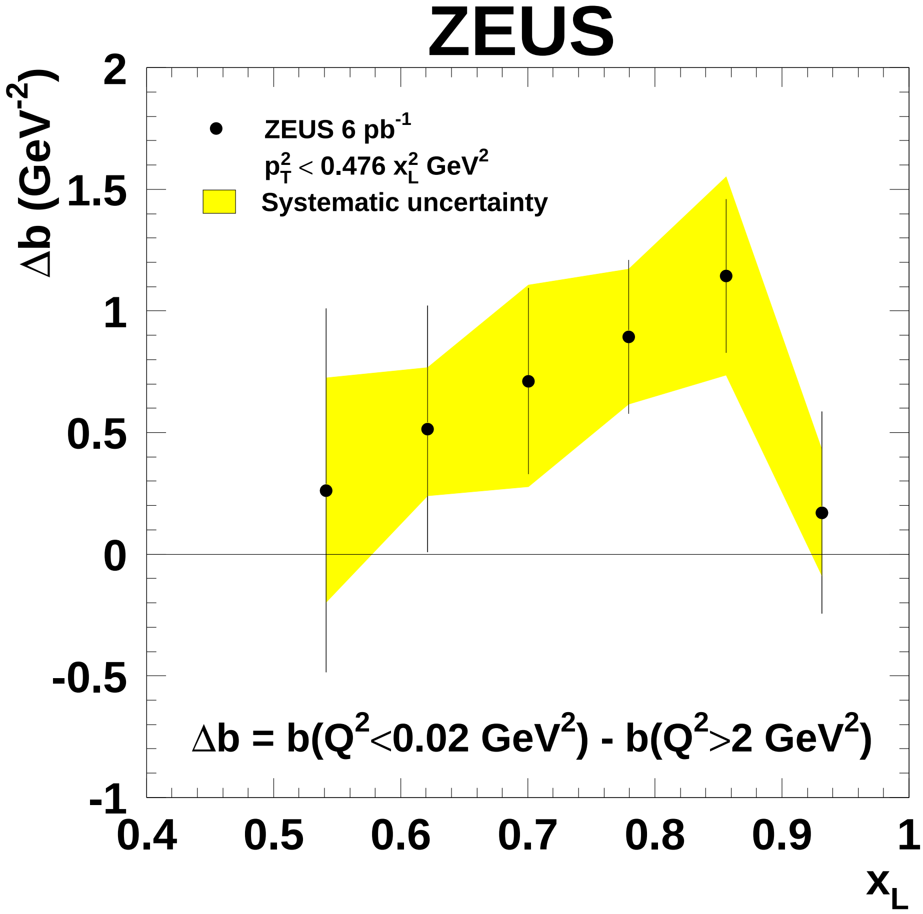

Figure 16: *The differences between the exponential slopes in photoproduction and DIS, Δb, versus x_L. The error bars show the statistical uncertainties; the shaded band shows the systematic uncertainties.*

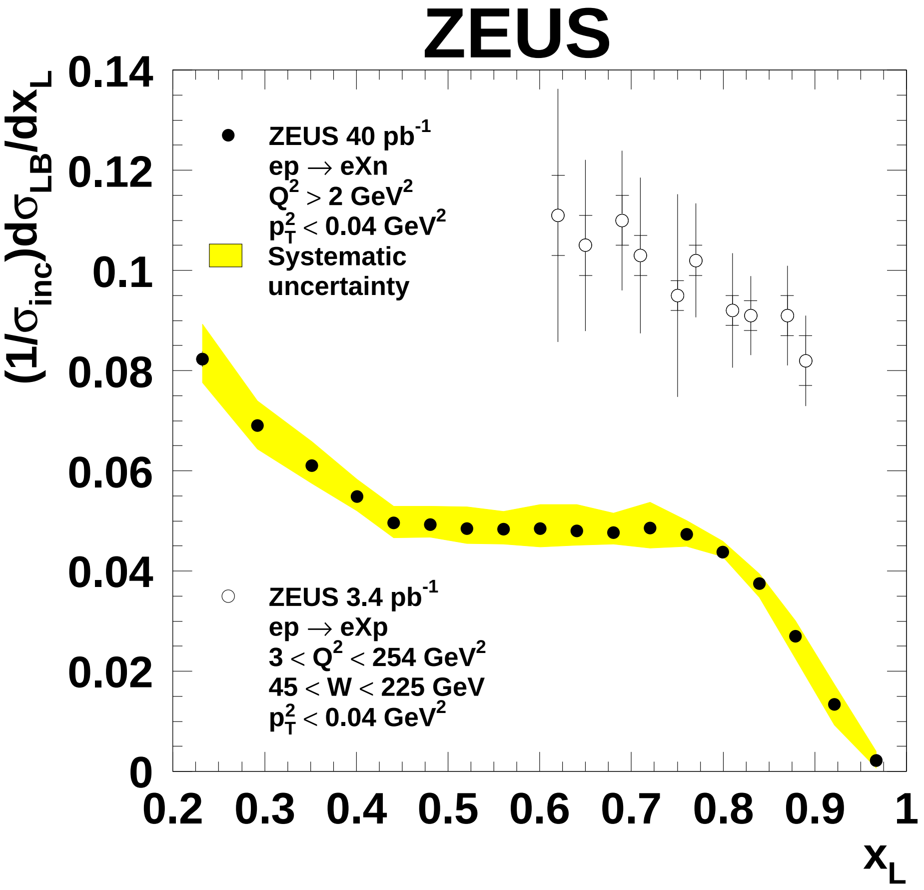

Figure 17: *The normalized differential distributions* $(1/\sigma_{\rm inc})d\sigma_{\rm LB}/dx_L$ *for leading protons and neutrons in the range* $p_T^2 < 0.04\ GeV^2$*. For the leading-neutron points, the statistical uncertainties are shown by a vertical error bar; in most cases they are smaller than the plotted symbol. The shaded band shows the systematic uncertainties; the band does not include the overall normalization uncertainty of* 2.1%*. For the leading-proton points, the inner error bars show the statistical uncertainty only; the full error bars show the statistical and systematic uncertainties added in quadrature.*

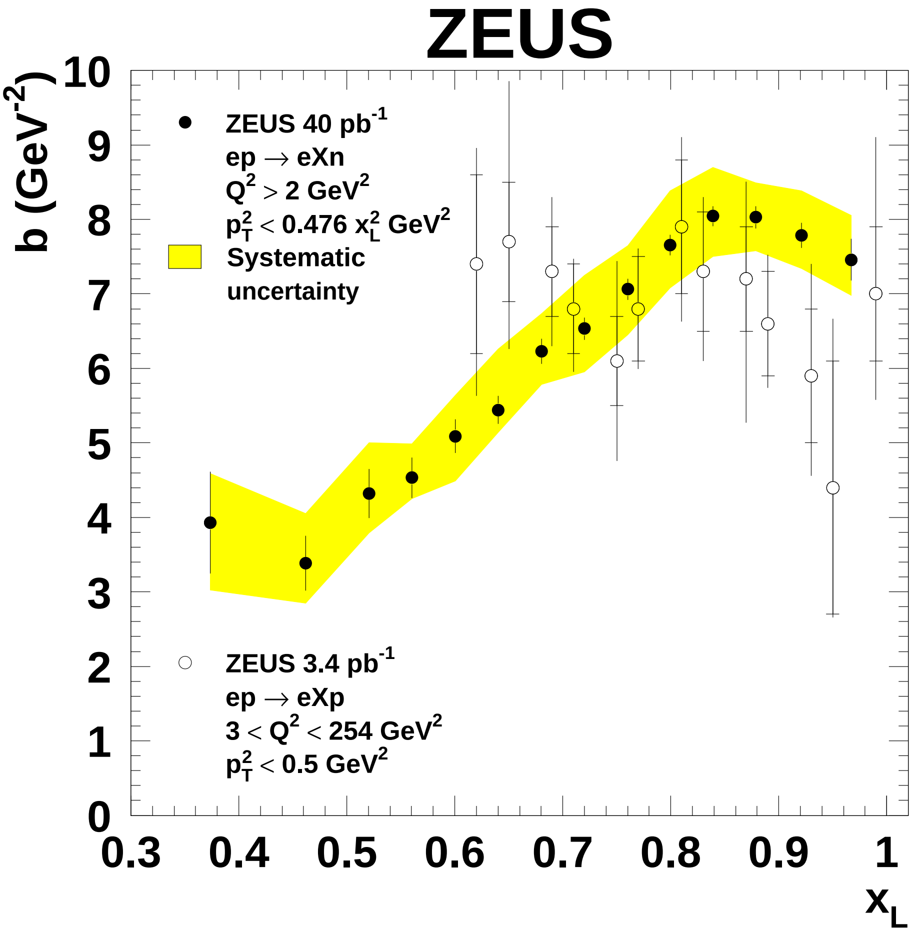

Figure 18: *The exponential slopes of the p_T^2 distributions for leading neutrons and protons in DIS. For the leading-neutron points, the error bars show the statistical uncertainties; the shaded band shows the systematic uncertainties. For the leading-proton points, the inner error bars show the statistical uncertainty only; the full error bars show the statistical and systematic uncertainties added in quadrature.*

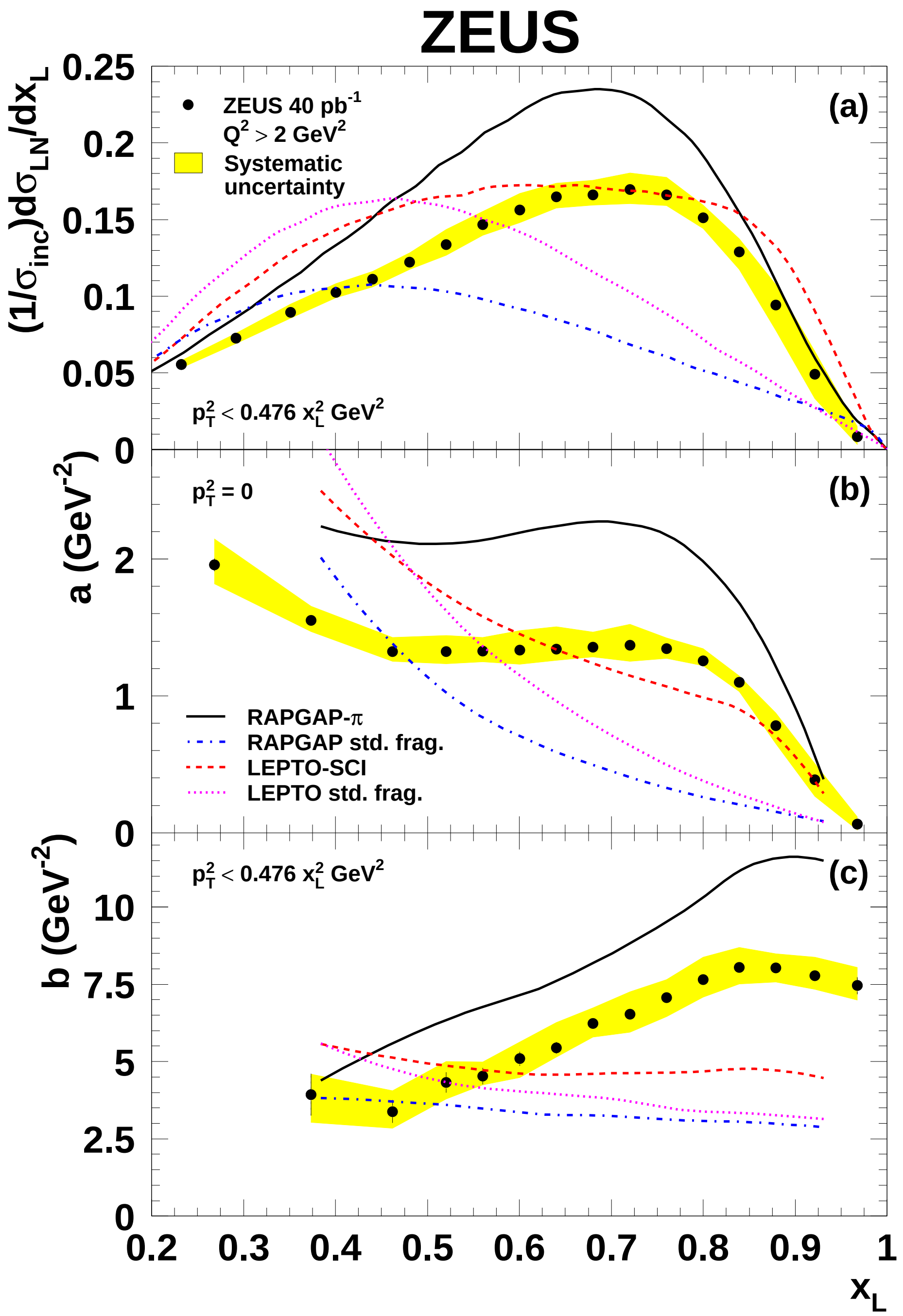

Figure 19: *Comparison to Monte Carlo models of DIS: (a) x_L distributions, (b) intercepts, and (c) exponential slopes. The error bars show the statistical uncertainties; the shaded bands show the systematic uncertainties. The bands do not include the overall normalization uncertainty of* 2.1% *for the x_L distribution and intercepts. The curves are from the DIS Monte Carlo models* Rapgap *[24] and* Lepto *[28]. The curves labeled* RAPGAP std. frag. *and* LEPTO std. frag. *are the models incorporating only standard fragmentation. The curve labeled* RAPGAP-π *includes also Pomeron and pion exchange; the curve labeled* LEPTO-SCI *is the model including soft color interactions.*

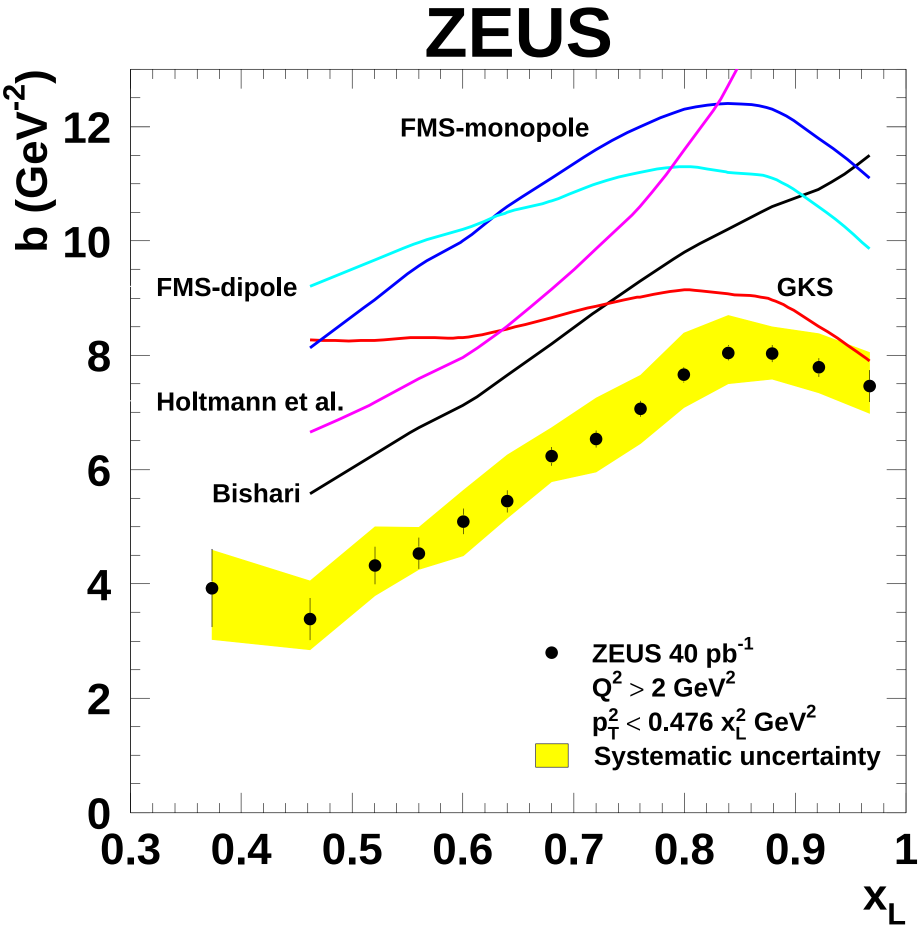

Figure 20: *The measured exponential slopes b compared to the predictions of models of one-pion exchange alone. The error bars show the statistical uncertainties; the shaded band shows the systematic uncertainties. The curves show predictions from the models discussed in the text [6–8].*

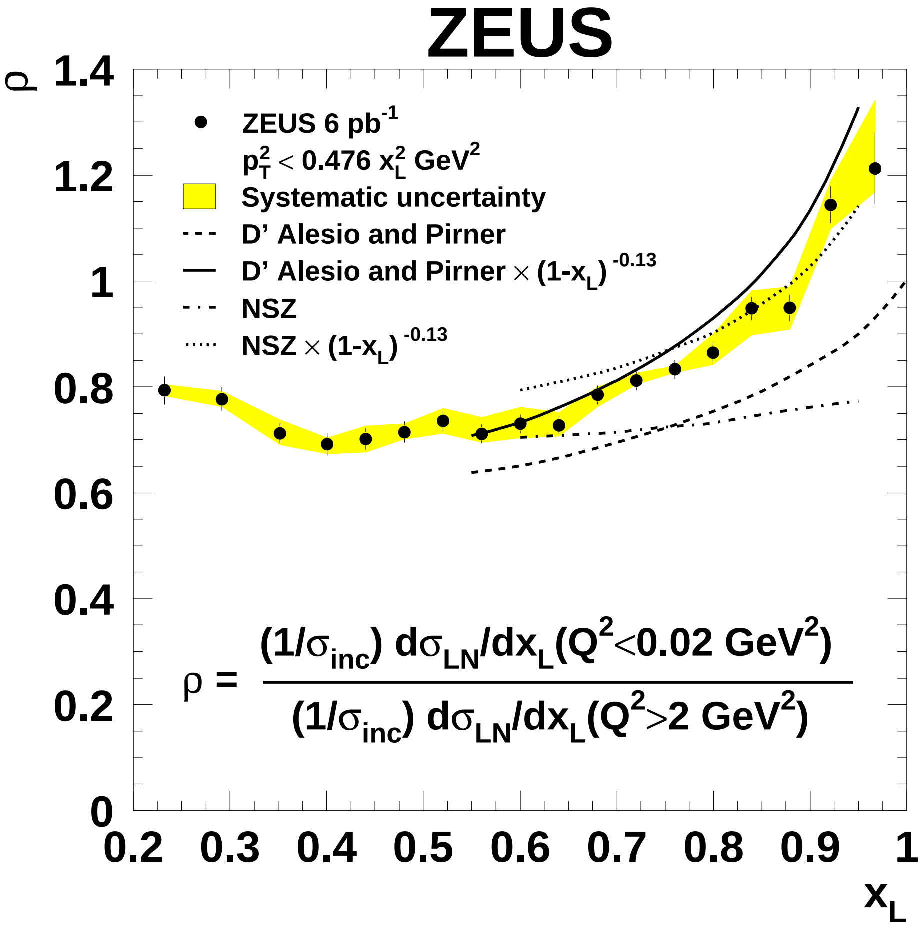

Figure 21: *Ratio of photoproduction and DIS x_L distributions. The error bars show the statistical uncertainties; the shaded band shows the systematic uncertainties. The band does not include the overall normalization uncertainty of* 5.1% *on the ratio. The dashed curve shows the neutron loss from a model of rescattering [14]; the solid curve is this model corrected for the different W dependence of the pion cross section in DIS and photoproduction. The dot-dashed curve shows the neutron loss from another absorption model [13]; the dotted curve is this model corrected for the different W dependence of the pion cross section in DIS and photoproduction.*

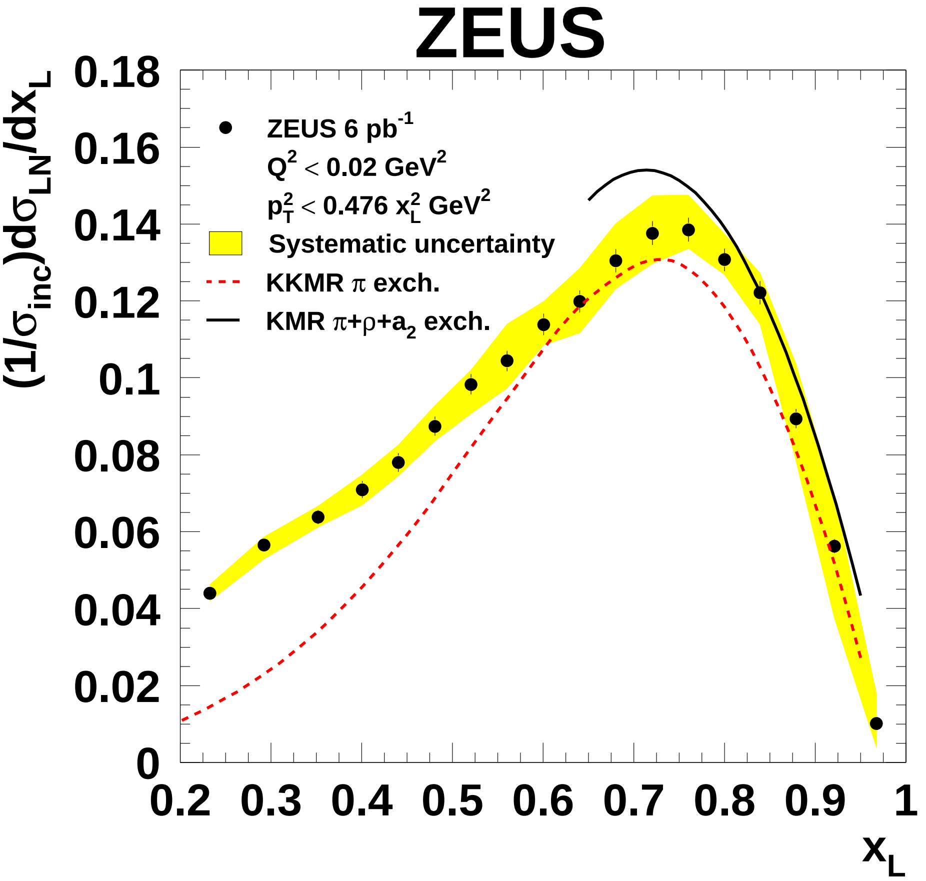

Figure 22: *x_L distribution for photoproduction. The error bars show the statistical uncertainties; the shaded band shows the systematic uncertainties. The band does not include the overall normalization uncertainty of 5.5%. The dashed curve shows the prediction of a model with enhanced neutron absorption and migration for pion exchange only [15]. The solid curve shows the same model including also ρ and a_2 exchanges [16].*

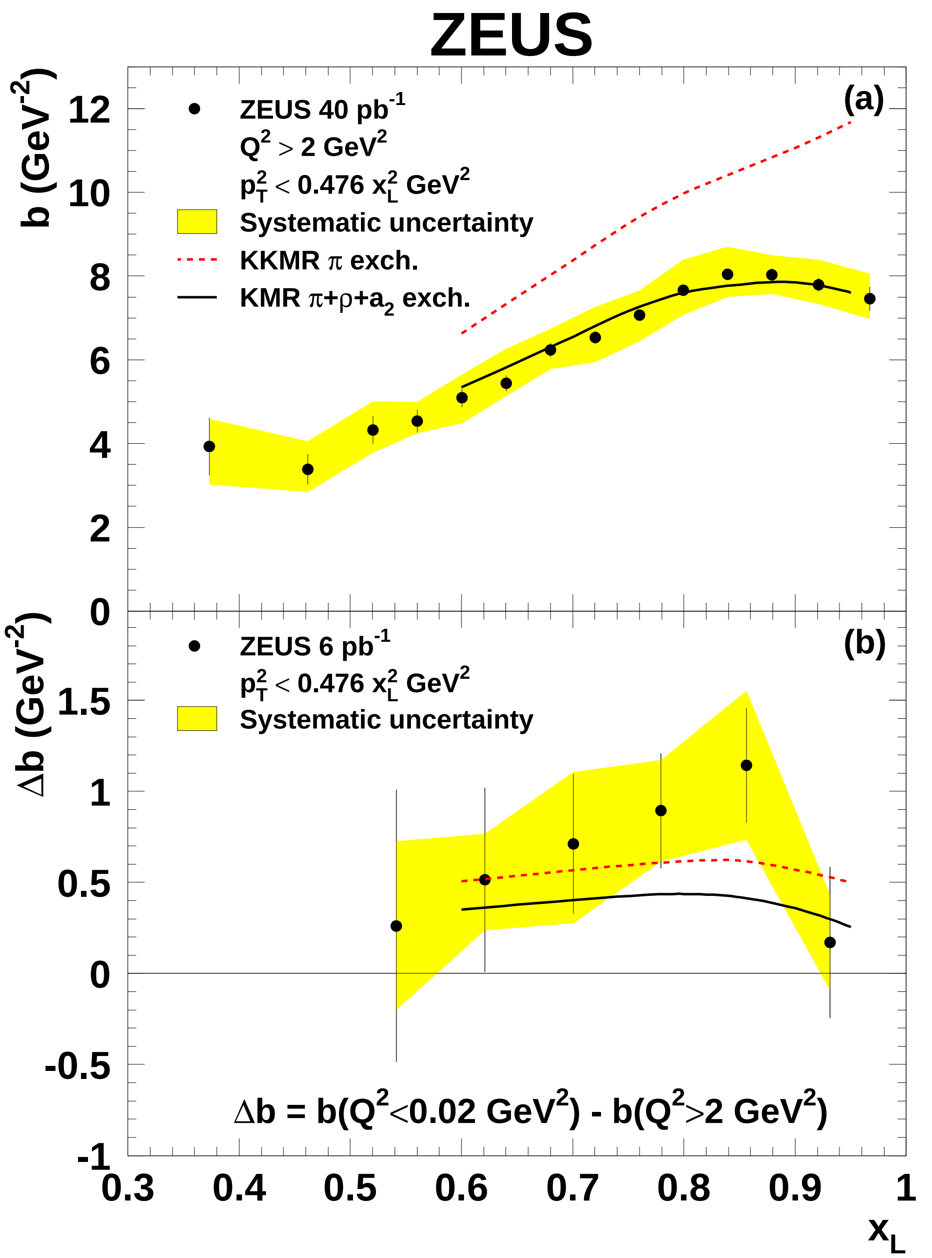

Figure 23: *(a) Exponential slopes b for DIS, and (b) difference of exponential slopes b for photoproduction and DIS. In both plots the error bars show the statistical uncertainties; the shaded band shows the systematic uncertainties. The dashed curves are from a model [16] based on pion exchange with enhanced neutron absorption and migration; the solid curves include also* ρ *and* a_2 *exchanges.*